Shared Transcriptomic Signatures Reveal Synaptic Pruning as a Link Between Alzheimer's Disease and Epilepsy

Huihong Li[1,2,3,4], Zhiran Xie[4], Yuxuan Tian[4], Bingying Lin[1,2,3,5], Jianwei Li[1,2,3,5], Jie Wu[1,2,3], Mingjie Chen[6], Xueke Liu[6], Yushan Sun[6], Si Chen[1,2,3,5], Zihan Deng[1,2,3,5], Mengqi Hong[1,2,3,5], Bing Huang[1,2,3,5], Naili Wei[1], Xiaoyu Ji[1,2,3,5*]

[1]Department of Neurosurgery, The First Affiliated Hospital of Shantou University Medical College, Shantou, Guangdong 515041, China

[2]Brain Function and Disease Laboratory, Shantou University Medical College, Shantou, Guangdong 515041, China

[3]Department of Pharmacology, Shantou University Medical College, Shantou, Guangdong 51504, China

[4]Program in Computational Biology and Biomedical Informatics, Yale University, New Haven, Connecticut, United States of America

[5]Pain and Related Diseases Research Laboratory, Shantou University Medical College, Shantou, Guangdong 515041, China

[6]Department of Biotechnology and Food Engineering, Guangdong Technion – Israel Institute of Technology, Shantou, Guangdong 515063，China

[*]Corresponding authors

Contact: Dr. Xiaoyu Ji, xyji@stu.edu.cn

Abstract

Alzheimer's disease (AD) and epilepsy (EP) exhibit a complex, bidirectional relationship, however, the molecular mechanisms underlying their comorbidity remain poorly understood. To address this gap, we analyzed large-scale transcriptomic datasets from pilocarpine-induced EP mouse models (n = 200), two AD mouse models expressing human tau (rTg4510) or amyloid precursor protein (J20) (n = 141), and transcriptomic profiles from AD and EP patient cohorts. Differential expression and weighted gene co-expression network analyses identified a highly conserved immune-related module enriched in microglia-specific genes, particularly *Tyrobp*, *Trem2*, and *C1q* complement component genes (*C1qa*, *C1qb*, *C1qc*) implicated in the synaptic pruning pathway. Gene regulatory network analysis showed that *Tyrobp* regulates these *C1q* components gene through *Trem2*. These hub genes were markedly upregulated in both models and human patient datasets, preserved their regulatory relationship across species, and displayed strong diagnostic value. Cell composition deconvolution and single-cell transcriptomics confirmed their high, cell-type-specific expression in microglia from both animal model and human patient datasets. Moreover, computational modeling indicated that excessive synaptic pruning, particularly of inhibitory synapses, alters the excitation/inhibition (E/I) balance toward excitability that increases neural network synchrony. Collectively, our findings reveal how microglial complement-driven synapse elimination may promote both seizure activity and cognitive decline. We suggest that microglia play a central role in

the comorbidity of EP and AD, and further exploration of this synaptic pruning pathway in the context of EP may provide promising insights into the treatment of AD and EP comorbidity.

Keywords: Alzheimer's disease, epilepsy, synaptic pruning, computational neuroscience, modeling, transcriptome, *Tyrobp*, *Trem2*, *C1q*

Graphic abstract

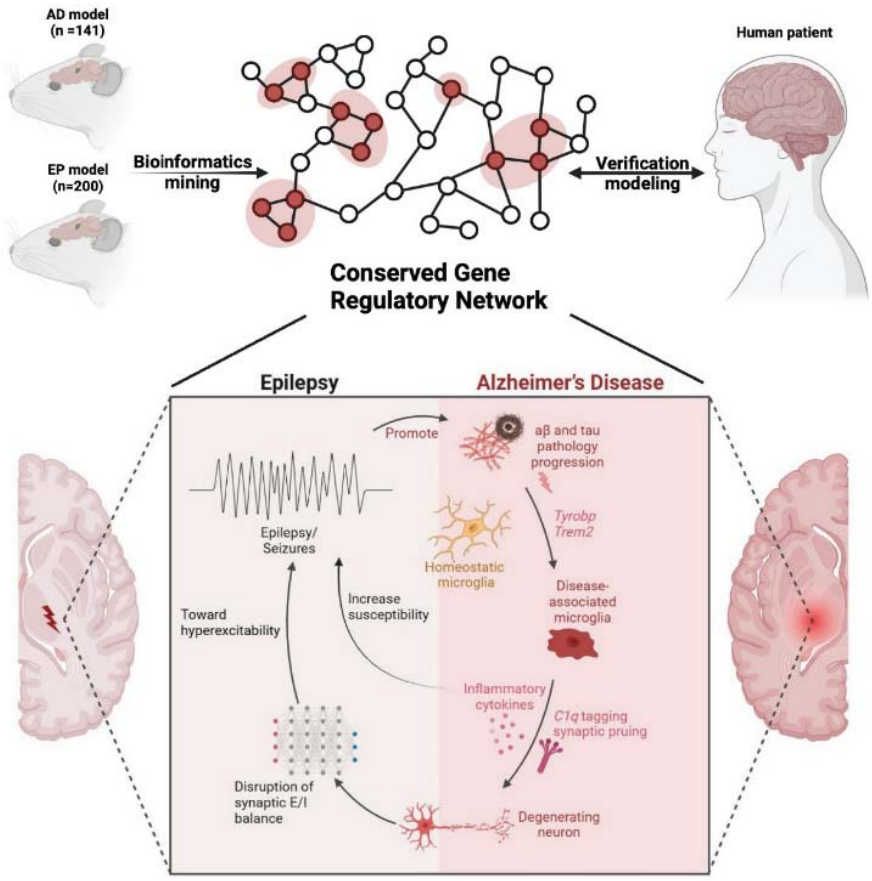

Highlights

- Transcriptomic analysis across epilepsy (EP) and Alzheimer's disease (AD) models and patient datasets revealed a conserved immune gene module.
- Shared transcriptomic signatures identified in animal models show strong diagnostic value in both AD and EP patient datasets.
- *Tyrobp-Trem2-C1q* microglial synaptic pruning pathway was identified as a central shared molecular mechanism across model and patient datasets.
- Computational modeling revealed that excessive synaptic pruning, particularly of inhibitory synapses, alters E/I balance toward excitability and increases synchrony in neural network.

1. Background

Alzheimer's disease (AD) and epilepsy (EP) are two common neurological diseases with a complex bidirectional relationship that contributes to their respective pathogenesis [1–3]. AD, characterized by progressive cognitive decline and neurodegeneration is the leading cause of dementia worldwide, affecting an estimated 55 million individuals. This number is projected to triple by 2050 as life expectancy increases [4]. EP, characterized by recurrent unprovoked seizures, affects over 50 million individuals worldwide with a particularly high incidence among elderly populations, especially those with neurodegenerative conditions such as AD [5,6].

Epidemiological studies demonstrate strong association between AD and EP. AD patients show increased susceptibility to EP, with 10–22% experiencing unprovoked seizures, while 22–54% demonstrating subclinical epileptiform activity during disease progression [7,8]. These seizures, predominantly occurring in the temporal lobe, correlate with accelerated cognitive decline and enhanced AD pathology [9]. Conversely, EP patients exhibit a two-fold higher risk of developing dementia compared to controls, with late-onset EP patients showing a three-fold increased risk [10,11]. This elevated risk is particularly evident in temporal lobe epilepsy (TLE), where numerous pathological features overlap with AD [9].

Both conditions share overlapping pathological features, particularly in TLE, including amyloid deposition, tau accumulation, and hippocampal sclerosis [12,13]. Chronic seizures increase neuronal activity and metabolic demands, potentially accelerating the production and aggregation of amyloid-β (aβ) and hyperphosphorylated tau protein [14,15]. Conversely, the progressive accumulation of these pathological proteins in AD may lower seizure thresholds, promoting hyperexcitability and epileptiform activity [16,17]. Furthermore, neuroinflammation, synaptic loss, and microglial activation, features of both AD and TLE, may synergistically accelerate neuronal damage and network dysfunction [18,19], potentially explaining the high comorbidity rates observed clinically.

The molecular mechanisms underlying this comorbidity remain incompletely understood, though mounting evidence suggests shared molecular pathways driving neuronal hyperexcitability and protein aggregation in both disorders [20]. Recent findings implicate dysregulated protein homeostasis, mitochondrial dysfunction, and chronic inflammatory responses as central contributors [7,18]. Additionally, alterations in glutamatergic and GABAergic signaling, alongside disruptions in synaptic plasticity pathways, appear to converge in both conditions, particularly within the hippocampal region [21].

Treating epilepsy in AD patients presents a complex clinical challenge, particularly regarding the decision to treat seizures and the selection of appropriate antiseizure medications [22]. Emerging therapeutic approaches, including targeted immunotherapies and novel small molecules, show promise but require a deeper understanding of the shared pathological mechanisms. Therefore, systems biology and computational modeling approaches are urgently needed to integrate insights from animal models and patients. Such approaches could reveal common molecular pathways, cellular processes, and neural network dynamics alterations underlying this comorbidity, which is crucial for developing more effective, targeted therapeutic strategies.

We hypothesize that conserved molecular mechanism exist in AD and EP animal models and human patients. To address this, we (1) analyzed and integrated large-scale transcriptomic data from pilocarpine-induced EP mouse models (n = 200), two AD mouse models expressing human tau (rTg4510) or amyloid precursor protein (J20) (n = 141) to identify shared transcriptional signatures and pathways; (2) validated these findings in AD and EP human patient datasets; and (3) developed computational models to link molecular insights to network mechanisms of epileptogenesis. Our analysis identified a conserved synaptic pruning pathway involving *Tyrobp*, *Trem2*, and *C1q* complement genes. Computational modeling further revealed that excessive synaptic pruning, particularly of inhibitory synapses, alters neural network toward excitability and increases synchrony.

2. Materials and Methods

2.1 Data Collection

A comprehensive database search was performed to retrieve transcriptomic data from both AD and EP models and human patients. Databases including Gene Expression Omnibus (GEO) and European Nucleotide Archive (ENA), were searched using the keywords “epilepsy” and “Alzheimer's disease”. We downloaded and analyzed large-scale bulk RNA-seq datasets from EP and AD mouse models. The EP model dataset was obtained from the ENA (PRJEB18790) and includes bulk RNA-seq data from 200 hippocampi of pilocarpine-induced EP model mice and wild-type (WT) control. The AD dataset was downloaded from GEO (GSE125957) and includes bulk RNA-seq data from 141 samples of the entorhinal cortex and hippocampus of AD model mice that expressed either human tau (rTg4510, TG) or amyloid precursor protein (J20), with their corresponding healthy controls at various ages (range from 2 to 12 months).

We also analyzed multiple large-scale transcriptome datasets from AD and EP patients to validate findings from animal models at the gene, pathway, and cellular levels. For cross-species validation of disease co-expression modules, we used 129 hippocampal samples from TLE patients (GSE63808) and 97 middle temporal gyrus samples from

AD patients (GSE132903). To evaluate the diagnostic value of shared transcriptional signatures, we analyzed 47 hippocampal samples from EP patients and controls (E-MTAB-3123), along with 253 different brain region samples from AD patients and controls (GSE48350). Finally, single-cell RNA sequencing (scRNA-Seq) data from 85,780 immune cells of six drug-refractory EP patients (GSE201048) and single-nucleus RNA sequencing (snRNA-Seq) data from 174,420 immune cells from 217 AD patients and 226 controls (GSE227223) were employed to identify the cell types and subtypes expressing these shared transcriptional signatures.

2.2 Quality control and preprocessing

All downloaded raw RNA sequences from AD and EP model datasets underwent quality control and trimming to obtain clean sequences, using FastQC (0.12.1) and Fastp (0.22.0) with stringent parameters (--qualified_quality_phred 30 --n_base_limit 5 --detect_adapter_for_pe --cut_tail --trim_front1 15 --dedup --trim_poly_x --trim_poly_g) to ensure high data quality [23,24]. Ribodetector (0.2.7) was used to remove potential rRNA contamination [25]. Low-quality regions in the sequences, attributed to instability in the sequencing platform, were also trimmed using Fastp. Trimmed sequences were then aligned to the GRCm39.111 reference mouse genome using HISAT2 (2.2.1) [26] and followed by quantification using featureCounts (2.0.6) [27].

For the AD model dataset, samples were excluded from subsequent analysis based on

the criteria outlined in the original publication, resulting in 121 high-quality RNA-seq samples. For the EP model dataset, duplicate and low-quality samples were initially removed. Then a variance-stabilizing transformation was applied to the count matrix before performing Principal Component Analysis (PCA) to identify potential outlier samples. PCA was then performed to identify outliers, with Mahalanobis distances calculated from PCA scores. A chi-squared distribution threshold of 0.975 was used to detect significant outliers, resulting in 11 samples subsequently excluded from analysis. Detailed information on quality control and mapping metrics is provided in **Table S1**. Following quality control, mapping, and exclusion of low-quality samples, no significant differences in read depth were observed between model groups and controls.

2.3 Differential Expression Analysis

Differential expression analysis was perform using DESeq2 (1.46.0) [28]. Before analysis, non-expressed and lowly expressed genes were filtered out to ensure that genes had at least 20 counts per sample in each design group. The DESeq function was then used to estimate size factors and dispersions and to perform statistical testing for differential expression [28]. For the EP model dataset, results were extracted by comparing the "EP" condition to the "WT" condition. For the AD dataset, we aimed to detect progressive differentially expressed genes (DEGs), as describe previously [29], using DESeq's likelihood-ratio test to fit the statistical model: *Gene expression* =

Genotype + *Age* + *Genotype*×*Age* (Interaction). p-values were adjusted for multiple testing using the Benjamini-Hochberg (BH) correction.

DEGs were identified based on an adjusted p-value < 0.05 and |log2 fold change| > 1. These thresholds were applied to the EP model dataset and to the final time point of the AD dataset. Shared DEGs between the EP and AD model datasets were identified by taking the intersection of their DEG results. Kyoto Encyclopedia of Genes and Genomes (KEGG) pathway and gene ontology (GO) analyses for shared DEGs were performed using WebGestalt (2024), with weighted set cover redundancy removal [30].

2.4 Weighted Gene Co-expression Network Construction

To construct weighted gene co-expression networks and compare results from EP and AD model datasets, we employed a standard meta-WGCNA comparison method [31–33]. This method is particularly suitable for comparative analysis across datasets to identify conserved gene modules, thus resolving batch effects between datasets. All datasets underwent variance-stabilizing transformation using DESeq2 (1.46.0) to normalize the variance across different samples. We then calculated the median absolute deviation (MAD) and retained the top 85% of genes with the highest MAD in each dataset, resulting in 10,997 genes common to all datasets for comparability in further analyses. Outliers were identified through hierarchical clustering, excluding two samples from the TG dataset and three from the J20 dataset. To assess dataset

comparability, general network properties such as average gene expression and overall network connectivity were calculated.

We constructed signed co-expression networks using the WGCNA R package (1.73) [32], selecting the lowest soft-thresholding power (β = 9) to achieve a scale-free topology fit index (R^2) of at least 0.85 across datasets. Adjacency matrices were generated using the signed network option and converted to topological overlap matrices (TOM) to quantify similarity in gene connectivity profiles. Modules were identified by average linkage hierarchical clustering of TOM dissimilarity (1-TOM), followed by dynamic tree cutting with parameters deepSplit = 2 and minClusterSize = 24. This procedure was also applied to patient microarray datasets (GSE63808 and GSE132903), using variance-stabilizing normalization with the “limma” (3.62.1) package [34].

To match modules between EP and AD model datasets, we color-mapped the AD modules to the best matching EP modules according to the hypergeometric test [31]. Module profiles were summarized using module eigengenes (MEs), derived from the first principal component of each module. To identify modules significantly associated with disease genotypes (EP or interaction of TG/J20), we calculated Pearson correlation coefficients between MEs and genotype information, with significance defined as $p < 0.05$ and an absolute correlation coefficient > 0.65 [35].

Module membership (MM) and gene-genotype significance (GS) were also determined by calculating Pearson correlations between individual genes and MEs or genotypes, respectively. KEGG pathway and GO analyses for module annotation were conducted using WebGestalt (2024) with weighted set cover redundancy removal [30].

2.5 Module Preservation Analysis

To assess module preservation of the EP model module in AD model datasets, we used two approaches [36]: Zsummary preservation statistics and cross-tabulation-based preservation statistics.

We employed the modulePreservation function from the WGCNA R package, with parameters set to networkType = "signed", nPermutations = 100, to calculate composite Z-summary preservation statistics. This metric evaluates preservation based on module size, network density, and connectivity, offering a comprehensive assessment of how well the structure of EP modules is maintained in AD datasets. The Z-summary thresholds were interpreted as follows: Z-summary > 10 indicates strong evidence of preservation, 2 < Z-summary < 10 suggests moderate evidence, and Z-summary < 2 indicates no evidence of preservation [36]. To complement the Z-summary statistic, we also used the medianRank preservation statistic, which assesses relative preservation across modules with less dependency on module size. A lower median rank denotes stronger observed preservation [36].

Additionally, we used a cross-tabulation method to examine module overlap between EP and AD model datasets, as well as between model and patient datasets (GSE63808 and GSE132903). This method generates a contingency table reporting the overlapping gene number between each module in the reference and test datasets [36]. The statistical significance of overlaps was assessed using Fisher's exact test, with p-values adjusted using the BH correction. A module was reported as significantly overlapping if the overlap count was > 30 and the adjusted p-value was < 0.05.

2.6 Hub Gene Identification and Regulatory Network Analysis

Hub genes act as key drivers within a module and were identified using stringent criteria to minimize false positives: genes ranking in the top 10% for intramodular connectivity within each module, MM > 0.9, and GS > 0.4. Shared hub genes were determined by intersecting the hub genes of key modules in both EP and AD datasets, along with the DEGs. The expression and diagnostic value of these shared hub genes were further explored in the AD and EP patient datasets (GSE48350 and E-MTAB-3123).

To explore interactions and potential regulatory relationships among shared hub genes in the EP and AD model datasets, we constructed a protein-protein interaction (PPI) network using the STRING database (12.0) (https://string-db.org/cgi/input.pl) with a

confidence score threshold of 0.4 and a false discovery rate (FDR) of 5% [37]. We then performed regulatory network analysis with the GENIE3 (1.28.0) algorithm, which applies a random forest approach to infer potential regulatory relationships from gene expression data. GENIE3 ranks regulatory interactions by weight, with higher weights indicating stronger regulatory links [38]. Gene expression profiles of the key module from the EP and TG model datasets were used to infer plausible regulatory interactions among shared hub genes. To reduce false positives, a weight threshold of 0.01 was applied to filter out weaker regulatory links. Additionally, only the top 30 plausible regulatory links between shared hub genes were retained to construct gene regulatory networks. Finally, the shared regulatory network of hub genes was constructed by intersecting the regulatory networks inferred from the EP and TG model datasets.

2.7 Machine Learning

To validate the diagnostic value of the transcriptomic signatures identified in animal models, multiple machine-learning models were used to train diagnostic models based on these signatures in EP and AD patient datasets (GSE48350 and E-MTAB-3123) to predict disease status based on gene expression profiles. The main goal was to distinguish patients with AD or EP from healthy controls. First, the gene expression data was standardized by applying the StandardScaler function in the sklearn.preprocessing module in Python. Standardization ensures that all

features/gene signatures have a mean of 0 and a standard deviation of 1, making them comparable across scales. Several machine learning algorithms were used in the classification process, including logistic regression, support vector machine (SVM), random forest, naive Bayes, XGBoost, AdaBoost, and CatBoost. To evaluate the performance of each model, a 5-fold stratified cross-validation method was used. Different metrics were used to measure the performance of the models, including accuracy, precision, recall, F1 score, and AUC. The ROC curve and AUC score for each classifier were plotted to visually examine the trade-off between sensitivity and specificity.

2.8 Cell Composition Deconvolution

In silico deconvolution can estimate the cellular composition of a tissue sample from its gene expression profile, with CIBERSORT particularly suited for cellular composition deconvolution of brain transcriptomes [39,40]. The raw count expression matrix was converted to FPKM values using edgeR (4.4.1) [41], followed by cell composition deconvolution using CIBERSORT (1.04**)** via the BrainDeconvShiny platform, with cell-type signatures specific to *Mus musculus* from immunopurified mouse brain tissue [40,42]. For statistical analysis, the Mann-Whitney test ($p < 0.05$) was applied to compare the EP dataset with the control group, while the Kruskal-Wallis test was used for the AD datasets, followed by pairwise comparisons across age and genotype groups. The BH method was used to control the FDR ($q <$

0.05). Associations between identified cell types and shared hub genes were determined by calculating Pearson correlation coefficients.

2.9 Single-cell and Single-nucleus RNA Sequencing Data Analysis

To localize and validate the expression of transcriptomic signatures identified in animal models at the cellular level in AD and EP patients, count matrices of sc/snRNA-seq (GSE201048 and GSE227223) were downloaded and processed according to the methods outlined in the original publications [43–45]. Quality control was performed to filter cells with high mitochondrial content (>20% for the EP dataset and >5% for the AD dataset) and select cells based on cellular complexity (300–5,000 genes per cell for the EP dataset and >500 genes for the AD dataset). Subsequent data processing was conducted using the standard Seurat pipeline, including scaling, normalization, variable gene identification, and clustering. PCA was performed on the 2,000 most variable genes, with the first 20 principal components (PCs) used for t-SNE and clustering in the EP dataset, and the first 30 PCs used for the AD dataset. Cluster identities were determined by identifying DEGs with the FindMarkers function, followed by annotation based on the original publications.

2.10 Computational modelling

To explore the contribution of the identified key pathways to pathological changes in

AD and EP at the network level, we implemented a spiking neural network using the Izhikevich neuron model to simulate hippocampal CA3 circuit dynamics with simulation spans of 1000ms, employing the Brian2 package [46]. The network consists of 1000 Izhikevich neurons (800 excitatory and 200 inhibitory), with dynamics governed by [47]:

$$\frac{dv}{dt} = 0.04v^2 + 5v + 140 - u + I$$

$$\frac{du}{dt} = a(bv - u)$$

where v is the membrane potential, u is the recovery variable. When v≥30 mV, the following reset conditions are applied:$v = c;\ u = u + d$. Parameters a, b, c and d are set to standard regular spiking for excitatory neurons and fast-spiking for inhibitory neurons following the Izhikevich framework [47]. I is external input incorporating both suprathreshold Poisson noise at 1 Hz and presynaptic inputs [47].

Following Liu's EP network modeling, synaptic connectivity is sparse, with a 0.1 probability of random connections between neurons, and interactions are modeled using conductance-based synapses to allow for voltage-dependent temporal and spatial summation [47]. Synaptic interactions simulate AMPA (excitatory) and GABA-a (inhibitory) currents for four connection types: excitatory-excitatory (E→E), excitatory-inhibitory (E→I), inhibitory-excitatory (I→E), and inhibitory-inhibitory (I→I) [47]. Synaptic currents are calculated as [48]:

$$I_j = wS_{i\to j}(t)\left(E_i - v_j\right)$$

we introduce w to leverage the synaptic weight, while $S_{i\to j}(t))$ is the synaptic conductance evolving as $\frac{dS_{i\to j}(t)}{dt} = -\frac{S_{i\to j}(t)}{\tau(i)}$ and E_i is the synaptic reversal potential [47]. Synaptic conductance is updated upon presynaptic spikes by adding a peak conductance $S_{i\to j}(max)$, while we calibrate unitary synapse to induce EPSPs for E→E/E→I and IPSPs for I→E/I→I of 1.0, 2.5, −2.0, −1.0 mV with time constants:$\tau = \{3, 3, 5, 5\}$ ms and reversal potentials:$E = \{0, 0, -75, -75\}$ mV [49–51]. Each of four types of synaptic weights (w) is drawn independently from a standard normal distribution, normalized to [0, 1], and set to 0 during synaptic pruning. We simulated synaptic pruning by selectively removing excitatory (E→E and E→I) or inhibitory (I→E and I→I) synapses, starting with those having the lowest weights based on the synaptic weight distribution (ranging from 0% to 50%, with 5% increments). Each pruning simulation was repeated at least 50 times.

The excitation/inhibition (E/I) ratio quantifies the balance between synaptic drives in the network, indicating firing rate stability, while event synchrony measures temporal coordination of firing patterns, implying network oscillation patterns. Both large E/I ratio and excessive synchrony are associated with EP and AD [48].

To analyze the network, we calculated the E/I ratio and event synchrony to measure the effects of synaptic pruning on firing rate stability and temporal coordination. The E/I ratio compares total excitatory currents (from E→E and E→I synapses) to the

absolute magnitude of inhibitory currents (from I→E and I→I synapses), averaged over the simulation period T [48]:

$$E/IRatio = \frac{\sum_{i=1}^{N} I_i^E(t)}{\left|\sum_{i=1}^{N} I_i^I(t)\right|}$$

where:

$I_i^E(t)$ represents excitatory synaptic currents onto neuron i at time t

$I_i^I(t)$ represents inhibitory synaptic currents onto neuron i at time t

N is the total number of neurons

$\bar{x}$ represents the mean over time T

Event synchrony (ES) quantifies spike timing coordination between excitatory neuron pairs by calculating the fraction of their spikes occurring within 5-ms windows. For each excitatory neuron pair (i, j), synchronous events are counted (with exact coincident spikes weighted by 0.5 and near-coincident spikes within the time window weighted by 1.0), then normalized by the geometric mean of both neurons' total spike counts [52]. During total simulation time T:

$$ES_{ij} = \frac{\sum_{s_i \in S_i} \sum_{s_j \in S_j} C\left(s_i, s_j\right)}{\sqrt{N_i N_j}}$$

where:

Si is the set of all spike times from neuron i during the simulation.

Sj is the set of all spike times from neuron j during the simulation.

Ni and Nj are the total number of spikes from neuron i and j respectively over the entire simulation period.

C(si, sj) counts synchronized events for each pair of spikes:

$$C(s_i, s_j) = \begin{cases} 1 & if\ 0 < |s_i - s_j| < 5ms \\ 0.5 & if\ s_i = s_j \\ 0 & otherwise \end{cases}$$

The network-wide event synchrony is computed as:

$$\text{Network ES} = \frac{1}{P}\sum_{i,j} ES_{ij}$$

Where $P = \frac{\text{Ne (Ne}-1)}{2}$ is the total number of unique excitatory neuron pairs, Ne is the number of excitatory neurons.

Both E/I ratio and ES values are normalized to baseline unpruned values to highlight pruning-induced changes in network dynamics. After normalization, the E/I ratio and ES value fluctuate around 1. A value greater than 1 means a higher E/I ratio or ES value than after synaptic pruning, and a value less than 1 means a smaller E/I ratio or ES value after synaptic pruning. For statistical analysis, we conducted a correlation analysis by calculating Pearson correlation coefficients and linear regression analysis to quantify the effect sizes of excitatory and inhibitory pruning on E/I ratio and synchronization.

3. Results

3.1 Identification and Functional Enrichment of Shared DEGs

3.1.1 Differential Expression Analysis

To reveal the shared molecular signatures underlying EP and AD models, we performed differential expression analysis using DESeq2. In the EP dataset, we identified 378 DEGs, with 351 upregulated and 27 downregulated genes (**Fig. 1A**). The TG dataset yielded 426 progressive DEGs, including 377 upregulated and 49 downregulated genes (**Fig. 1B**). In contrast, the J20 dataset contained only one upregulated progressive DEG, Cst7 (**Fig. 1C**). Notably, 101 genes were differentially expressed in both the EP and TG datasets, representing 26.72% and 23.71% of the DEGs in each dataset, respectively (**Fig. 1A–B**). This substantial overlap suggests shared molecular pathways between EP and TG models. Detailed DEGs information is available in **Table S2**.

3.1.2 Functional Enrichment Analysis of Shared DEGs

To investigate the biological relevance of these shared DEGs between EP and TG models, we conducted a functional enrichment analysis. KEGG pathway analysis identified several most enriched pathways, including “complement and coagulation cascades,” “phagosome,” and “cytokine-cytokine receptor interaction” (**Fig. 1D**). GO enrichment analysis highlighted key biological processes, such as “defense response,”

"immune response," and "regulation of cytokine production" (**Fig. 1E**). Additionally, enriched molecular functions included "signaling receptor binding" and "immune receptor activity," with cellular components such as the "extracellular matrix" and "side of membrane" also significantly represented. These findings indicate that the shared DEGs are primarily involved in immune processes, reflecting shared molecular pathways in both EP and TG models. Detailed GO enrichment analysis results can be found in **Table S2**.

3.2 Construction of Weighted Gene Co-Expression Network

WGCNA was particularly suited for this study due to its ability to identify modules of highly correlated genes and reveal underlying biological pathways conserved across different conditions. By applying WGCNA to both EP and AD datasets, we aimed to identify conserved gene modules that may represent common molecular mechanisms between EP and AD.

After filtering out outlier samples, low-expression, and low-variance genes in each model dataset, we retained 10,997 genes common to all model datasets for further analysis (**Fig. S1A-C**). For network construction, we selected a soft-thresholding power of 9 to ensure that networks in all model datasets exhibited scale-free topology with a fit index > 0.85 (**Fig. S1D**). This threshold was consistently applied across analyses to maintain network comparability. To assess comparability between EP and

AD model networks, we examined correlations of ranked mean gene expression and ranked gene connectivity between dataset pairs. For EP and J20 model datasets, high correlations were observed for both expression ($r = 0.98$, $p < 1e-200$) and connectivity ($r = 0.23$, $p < 5.7e-132$). Similarly, EP and TG model datasets showed significant correlations (expression: $r = 0.96$, $p = 1e-200$; connectivity: $r = 0.43$, $p = 1e-200$) (**Fig. S1E**), indicating comparability across model datasets [31].

We used the WGCNA package to construct gene co-expression networks for the EP, TG, and J20 model datasets. The analysis identified diverse gene modules across the three models: the EP dataset revealed 33 modules (28–790 genes per module) (**Fig. 2A**), TG had 29 modules (34–1,537 genes) (**Fig. 2B**), and J20 contained 32 modules (27–613 genes) (**Fig. 2C**). Detailed module information can be found in **Table S3**. Associations between MEs and model genotypes were assessed. The EP model dataset identified seven modules significantly associated with the EP genotype: three with positive correlations (green, steelblue, turquoise; $0.73 \leq r \leq 0.79$, $p < 3e-31$) and four with negative associations (lightyellow, red, lightcyan, paleturquoise; $-0.92 \leq r \leq -0.69$, $p < 8e-27$). Notably, five of these modules contained DEGs linked to the EP genotype (turquoise: $n = 198$, green: $n = 86$, steelblue: $n = 12$, lightcyan: $n = 12$, red: $n = 5$) (**Fig. 2A, D**). In the TG model dataset, seven modules showed significant associations with the TG genotype: two with positive correlations (turquoise, yellow; $0.72 \leq r \leq 0.87$, $p < 3e-10$) and five with negative associations (brown, saddlebrown, darkorange2,

darkmagenta, royalblue; $-0.83 \leq r \leq -0.67$, $p < 1e-08$). Nine modules contained DEGs associated with the TG genotype (turquoise: n = 268, yellow: n = 14, green: n = 7, darkorange2: n = 4, blue: n = 2, orangered4: n = 2, royalblue: n = 2, darkmagenta: n = 1, tan: n = 1) (**Fig. 2B, E**). Consistent with the DEGs analysis that showed the J20 model dataset had fewer DEGs, none of the modules exhibited significant associations with the J20 genotype ($r < 0.4$) (**Fig. 2C, F**).

3.3 Module Preservation Analysis

Following module construction, we assessed the preservation of EP model modules in the AD model datasets to reveal conserve molecular pathways between EP and AD models. Our analysis revealed varying degrees of module preservation between EP and AD model datasets (**Fig. 3A-B**). In the TG model, the steelblue module had low preservation scores (Z-summary.pres = 0.89. Similarly, in the J20 model, the steelblue and yellow modules showed weak preservation (Z-summary.pres < 4), suggesting these may represent unique biological processes specific to the EP model dataset. In contrast, several EP model modules, including green, blue, and brown, exhibited high preservation scores and significant overlap with AD modules in both models, suggesting they represent conserved biological processes. Preservation statistics are shown in **Table S3**.

Notably, the turquoise EP model module had the highest preservation scores

(Z-summary.pres = 83.01) and showed strong overlap with the TG model turquoise module, displaying the highest overlap counts and the lowest adjusted p-values (**Fig. 3A, C**). Both turquoise modules were positively correlated with disease genotype (EP: r = 0.79, p = 5e-41; TG: r = 0.87, p = 4e-18) and contained most DEGs in each model (**Fig. 2A, C**). Notably, this module is less conserved in the J20 model (**Fig. 3B**, **Table S3**), suggesting that this module is a result of changes in gene expression in the EP and TG model rather than being universal across different datasets like green, blue, and brown module (**Fig. 3A-B**, **Table S3**). Other EP modules, such as lightcyan, showed significant correlations but did not display preservation. GO enrichment analysis of this model turquoise module revealed enrichment in immune-related terms (**Table S3**). We further assessed the preservation of the mouse turquoise module in EP and AD patient dataset (GSE63808 and GSE132903), finding that the turquoise immune modules from EP and TG models significantly overlapped with modules constructed from EP and AD patient datasets, respectively (**Fig. 3E-F, S2**). This suggests the turquoise module represents a conserved immune molecular signature across species and disease states, suggesting that immune processes play a preserved and significant role in these modules across conditions.

3.4 Shared Hub Gene Identification and Regulatory Network Analysis

To identify hub genes that may play a crucial role in both EP and AD, we intersected the hub genes of the turquoise module from EP and TG model datasets with the

previously identified 101 DEGs. This analysis identified 19 shared hub genes common to both conditions (two shared hub genes not shown in the figure due to their ranking: *Apobec* and *Cxcl16*) (**Fig. 4A-B**). We then constructed a PPI network to investigate the biological significance of these 19 genes and the results showed a PPI network consisting of 14 genes **(Fig. 4C, Table S4**). This PPI network revealed strong connectivity among *C1q* complex component genes (*C1qa*, *C1qb*, *C1qc*) and other immune-related genes, including *Trem2*, *Tyrobp*, and *Adgre1*. GO biological process enrichment analysis highlighted the most significant processes involved in "Synaptic pruning" (**Fig. 4D, Table S4**). Genes involved in "Synaptic pruning" (*C1qc*, *C1qb*, *C1qa*, *Trem2*) also participate in other enriched processes, such as "Complement-mediated synapse pruning" (*C1qa*, *Trem2*) and "Microglial cell activation" (*Tyrobp*, *C1qa*, *Trem2*) (**Table S4**).

While WGCNA reveals gene co-occurrence patterns, it does not identify regulatory mechanisms. To explain potential regulatory relationships among these 19 genes, we applied the GENIE3 algorithm to gene expression profiles of the turquoise module in both EP and TG conditions (**Table S5**). By intersecting predicted regulatory networks from both conditions, we identified a shared regulatory pathway: *Tyrobp* regulates *Trem2*, which in turn regulates the complement component genes *C1q* via *C1qa* (**Fig. 4E**). These genes, particularly *Tyrobp*, *Trem2*, and *C1q* complex components gene (*C1qa*, *C1qb*, *C1qc*), play central roles in co-expression modules of both EP and TG

model and are involved in multiple enriched terms, especially synaptic pruning. Notably, these genes are also progressive DEGs in the TG model (**Fig. 4F**). The successful reconstruction of a regulatory network involving *Tyrobp*, *Trem2*, and *C1q* component genes suggests they may represent a conserved molecular pathway underlying both conditions.

3.5 Validation of the Diagnostic Value of Shared Hub Genes

To validate the clinical relevance of the identified transcriptional signatures in AD and EP animal models, we analyzed the expression of 19 shared hub genes in datasets from AD and EP patients (GSE48350 and E-MTAB-3123) compared to controls. Thirteen of these 19 genes were expressed in both datasets, with 10 exhibiting significantly higher expression levels ($p < 0.05$) compared to controls (**Fig. 5A-B**). Notably, genes such as *Tyrobp*, *Trem2*, and *C1q* complex component genes demonstrated pronounced significance in both datasets (**Fig. 5A-B**). To assess their diagnostic potential, we developed diagnostic models leveraging the expression profiles of these genes in the hippocampus (**Fig. S2**). Using multiple machine learning methods, these models effectively differentiated disease from control groups, with particularly high performance in the EP dataset (AUC > 0.9) and satisfactory performance in the AD patient dataset (AUC > 0.7) (**Fig. S3)**. These findings confirm the diagnostic value of the transcriptional signatures identified in animal models in human AD and EP patients.

Given that these genes were shared hub genes of co-expression modules in EP and AD models, likely reflecting conserved expression pathways and progressive changes, we examined their co-expression patterns in AD and EP patient datasets (GSE48350 and E-MTAB-3123) by calculating Pearson correlation coefficients. *Tyrobp*, *Trem2*, and the *C1q* component genes demonstrated strong correlations in both AD and EP patient datasets ($r > 0.85$), whereas co-expression patterns among other genes were less consistent across datasets (**Fig.5C-D**). Collectively, these findings suggested that synaptic pruning pathway genes such as *Tyrobp*, *Trem2*, and the *C1q* component are not only conserved between AD and EP animal models and human patients but also likely play critical roles in the underlying pathology of these conditions.

3.6 Cellular Composition Alteration and Genes Localization in Cell Type

To investigate cellular composition changes and their associations with the key hub genes (*Tyrobp*, *Trem2*, *C1q* complex genes) in TG and EP conditions, we employed CIBERSORT for cell composition deconvolution of bulk RNA-seq data. Our analysis revealed significant cellular composition alterations. Firstly, we observed a notable reduction in neuronal composition in both EP and TG conditions compared to controls ($p < 0.05$) (**Fig. 6A, C**). Secondly, there was a marked increase in microglial composition in both models ($p < 0.05$), consistent with the enrichment of immune-related processes identified in previous analyses (**Fig. 6A, C**). While

astrocyte and endothelial cell alterations were also detected in EP and TG models (at 8 months, $p < 0.05$), these changes were less pronounced than the neuronal decrease and microglial increase observed in the TG model (**Fig. 6A, C**). No significant differences were found in oligodendrocyte composition in either condition.

We examined the relationship between these cellular composition changes and the key hub genes such as *Tyrobp*, *Trem2*, and *C1q* complex genes by conducting Pearson correlation analyses (**Fig. 6B, D**). Notably, all key hub genes showed strong negative correlations ($r < -0.7$) with neuronal composition in both EP and TG conditions, suggesting an inverse relationship between their expression levels and neuronal proportion. Conversely, strong positive correlations were observed between these genes and microglial and endothelial cell composition ($r > 0.7$). Correlations with astrocytes and oligodendrocytes were more variable and showed less consistency across genes and conditions. Although no cellular composition changes were observed in the J20 model (**Fig. S4A**), we found that genes such as *Tyrobp*, *Trem2*, and *C1q* complex components, were strongly associated with microglial composition, indicating that these genes demonstrate a strong link with microglial cell types (**Fig. S4B**). We localized the expression of these genes to cell types using the whole mouse brain transcriptome cell type atlas from the Allen Brain Atlas [53]. The results showed that the majority (15 of 19 genes) were predominantly expressed in immune cells, particularly microglia and macrophages (**Fig. S5**).

To further explore the expression of these genes in human patient cell types, especially immune cells, we explored the expression of these genes in two large-scale sc/sn RNAseq datasets of immune cells from AD and EP patients (GSE201048 and GSE2272230) (**Fig. S6**). We found that 12 of the shared hub genes were detectable in both datasets. Among these, *Tyrobp* and *Trem2*, along with the *C1q* complex component genes, displayed notably high and predominant expression in microglia compared to other shared hub genes (**Fig. S6**). Collectively, these findings confirmed the high and predominant expression of *Tyrobp*, *Trem2*, and *C1q* components genes in the microglia of both AD and EP patients. This consistency between animal models and human patients suggests that microglia and these synaptic pruning genes play crucial roles in the progression of both AD and EP pathology and may represent a potential conserved regulatory pathway.

3.7 Computational modeling of synaptic pruning on neural network

To better understand how synaptic pruning influences neural network dynamics and its potential role in the comorbidity of AD and EP, we developed a neural network model simulating the hippocampal CA3 circuit. In this model, we systematically varied the extent of synaptic pruning (0% to 50%) at either excitatory or inhibitory synapses. We then quantified changes in the E/I ratio and synchronization levels, conducting at least 50 simulation runs per condition (**Fig. 7**).

Our findings indicate that pruning of either excitatory or inhibitory synapses alters the E/I ratio, with distinct effects. Inhibitory synaptic pruning significantly elevated the E/I ratio, while excitatory pruning reduced it. These trends were consistent across all simulations and in experiments where excitatory or inhibitory pruning was varied independently (**Fig. 7A**). Correlation analysis showed a negative association between excitatory pruning and the E/I ratio ($r = -0.474$) and a positive correlation between inhibitory pruning and the E/I ratio ($r = 0.684$) (**Fig. 7B**). Linear regression further confirmed that excitatory pruning reduced the E/I ratio ($\beta = -1.038$), whereas inhibitory pruning increased it significantly ($\beta = 1.454$), with the effect of inhibitory pruning surpassing that of excitatory pruning.

Interestingly, inhibitory pruning displayed a moderate positive correlation with event synchronization ($r = 0.346$), while excitatory pruning showed only a weak negative correlation ($r = -0.039$) (**Fig. 7B**). Linear regression analysis reflected this pattern, with inhibitory pruning exerting a stronger effect on synchronization ($\beta = 0.358$) than excitatory pruning ($\beta = -0.041$). Additionally, the E/I ratio itself was positively correlated with synchronization ($r = 0.491$) (**Fig. 7B**), suggesting that the influence of synaptic pruning on network synchronization may be nonlinear and indirectly mediated by changes in the E/I balance.

These simulations suggest that excessive synapses pruning alters the E/I ratio, and inhibitory pruning overpowering the effects of excitatory pruning and substantially enhancing synchronization.

4. Discussion

While Alzheimer's disease (AD) and epilepsy (EP) share a complex bidirectional relationship, the molecular pathways linking AD-related neurodegeneration to increased EP susceptibility remain poorly understood. To address this issue, we used rigorous bioinformatic and computational methods to integrate and analyze transcriptional data from multiple large-scale publicly available animal models and human patient datasets. We identified consensus molecular pathways, cellular processes, and neural network dynamics associated with this comorbidity across multiple datasets.

Conserved Neuroinflammation Pathways in Epilepsy and Alzheimer's Disease

Our findings provide strong evidence supporting the hypothesis that neuroinflammatory pathways are common between AD and EP, particularly those directly triggered by tau pathology [7,18]. Consistent with previous results, we identified no significant transcriptional changes in the J20 model due to the inherent characteristics of the model rather than technical limitations (**Fig. 1C**), such as slower and later accumulation of pathology and variable neuronal cell loss [29]. However,

differential expression analysis demonstrated significant gene overlap between EP and TG models (**Fig. 1A-B**). WGCNA revealed preservation of the immune-related turquoise module across both disease models as well as human patient datasets (**Fig. 2-3**). These results align with previous analyses of this dataset that identified significant conservation of this module across multiple AD patient cohorts [29]. Although highly conserved in the EP and TG datasets, the J20 dataset did not show strong preservation of this module (**Fig. 3B**), which further reinforces that this module is the result of a transcriptional state change that is conserved in EP and TG. We extended these findings by demonstrating the module's conservation and overlap in EP models and patient datasets, suggesting it represents a fundamental molecular pathway shared between AD and EP (**Fig. 3,5**).

Functional enrichment analysis of shared DEGs and the preserved module revealed significant enrichment in neuroinflammatory processes, including inflammatory response, cytokine production, blood vessel morphogenesis, glial cell activation, and complement and coagulation cascades (**Fig. 1D-E, Table S3**). Additionally, we observed increased populations of neuroinflammation-associated cell types, including astrocytes, microglia, and endothelial cells, in both TG and EP animal models (**Fig. 6**).

Neuroinflammation has been extensively documented in both conditions and appears

to serve a complex dual role in disease progression [54,55]. While activated microglia facilitate Aβ plaque clearance and reactive astrocytes provide metabolic support and ionic homeostasis that may attenuate neural damage and seizures, chronic activation or dysfunction of these glial populations can promote disease progression through persistent neuroinflammation [56–59]. Specifically, activated microglia and astrocytes secrete proinflammatory cytokines and chemokines, including IL-1β, TNF-α, and IL-6, which can enhance neuronal hyperexcitability, increase seizure susceptibility, exacerbate Aβ and tau aggregation, and accelerate neurodegeneration and cognitive decline [56–59] .

Additional inflammatory components, including complement cascade activation and blood-brain barrier (BBB) dysfunction, are implicated in both pathologies [60–63]. Complement activation contributes to synaptic loss in AD and is elevated in TLE patient tissue [62,63]. BBB disruption precedes neuronal hyperactivity in EP, promoting astrocyte dysfunction and seizures, while in AD it facilitates peripheral inflammatory cell infiltration, amplifying neuroinflammation [60,61].

These results establish neuroinflammation as a key mechanistic link between AD and EP [18]. AD-associated inflammation can enhance neuronal hyperexcitability and seizure susceptibility. Conversely, EP-induced inflammation may accelerate Aβ and tau accumulation, contributing to cognitive decline. Our results support previous

studies and suggest that neuroinflammation is highly conserved between these diseases and between species. Future studies should focus on revealing the precise causal relationship between these neuroinflammatory components and AD-EP comorbidity.

Synaptic Pruning was Identified as a Core Pathway in this Comorbidity

A comprehensive analysis of this conserved module revealed a central synaptic pruning pathway involving *Tyrobp*, *Trem2*, and *C1q* complement genes (**Fig. 4**). These genes demonstrated consistent upregulation across both AD and EP patient datasets, with preserved regulatory relationships in both animal models and human patients (**Fig. 5**). Moreover, we confirmed their specific expression in microglial cells across both animal and human patient samples (**Fig. S5-6**). Collectively, these findings suggest that microglia-mediated synaptic pruning represents a core mechanistic pathway underlying the comorbidity of AD and EP.

This pathway has been extensively documented in AD pathology, with its role extending to both tau and Aβ pathology [64]. Dysregulation or mutations in *Tyrobp* and *Trem2* are established risk factors for AD due to their effects on microglial function [65,66]. Under physiological conditions, microglia maintain synaptic homeostasis through a regulated process in which complement proteins, including *C1q*, tag unnecessary synapses for elimination [67]. Microglial receptors, particularly *Trem2* and

Tyrobp, recognize these tags and initiate phagocytic clearance, a process critical for neural circuit refinement and maintenance in the adult brain [68]. In AD pathology, these receptors enable microglia to recognize protein deposits, triggering their transition to a disease-associated microglial (DAM) state characterized by enhanced phagocytic activity and elevated expression of *Tyrobp*, *Trem2*, *Apoe*, and complement proteins including *C1q* [64]. While *Tyrobp* or *Trem2* deficiency disrupts DAM activation and impairs critical microglial functions such as plaque clearance, potentially accelerating AD pathology, this pathway overactivation can also contribute to neurodegeneration and cognitive decline through excessive *C1q*-mediated synaptic pruning [64,69–71].

Synaptic pruning can exert effects on both AD and EP disease progression through two primary mechanisms: synaptic transmission and synaptic plasticity. Regarding synaptic transmission, elevated *C1q* expression or Aβ accumulation in the CA1 region leads to decreased miniature and evoked excitatory postsynaptic currents [72,73]. In AD, this reduction in synaptic transmission contributes to cognitive decline by disrupting normal neural communication. For EP, this alteration affects both excitatory and inhibitory neurons [74], potentially contributing to the imbalance between excitation and inhibition that characterizes epileptic activity. Notably, these effects can be reversed through *C1q* downregulation [75,76].

The pathway's impact on synaptic plasticity is equally significant. Research

demonstrates that C1q inhibition in aged experimental models can restore both long-term potentiation (LTP) and long-term depression (LTD) [69,71,77]. In non-aged models, increased *C1q* expression also impairs the LTP process [74]. This is particularly relevant for AD, where impaired synaptic plasticity is a feature of cognitive decline. In EP, compromised synaptic plasticity may contribute to the formation and maintenance of epileptogenic circuits. The relationship between these mechanisms appears bidirectional: excessive synaptic pruning leads to neuronal damage and reduced LTP, which in turn promotes disease progression in both conditions, creating a harmful feedback loop where synaptic dysfunction promotes pathological processes.

Notably, interventions targeting this synaptic pruning pathway, whether through knockdown of regulatory genes such as *Tyrobp* and *Trem2* or direct inhibition of *C1q* accumulation, have successfully restored electrophysiological function and cognitive function in AD models, even in the presence of significant amyloid and tau pathology [64,69–71]. Our results establish a regulatory network that is consistent with previous observations and further extends its role in the comorbidity of AD and EP (**Fig. 4**).

While this pathway is extensively studied in the context of AD, to the best of our knowledge, no prior research has established a connection between this pathway and the comorbidity of EP and AD. Our understanding of the relationship between synaptic pruning and EP remains nascent, especially how to interpret its contribution

to the network dynamics [78]. To address this gap, we conducted an in-silico experiment to shed light on this issue.

Synaptic Pruning Alter E/I Balance to Promote Network Synchronization

Computational modeling has become an important tool for understanding AD and EP pathology, models ranging from molecular-level simulations of ion dynamics to large-scale network models [79,80]. Disruption of E/I balance and neural synchronization represent a key point of convergence between AD and EP pathology, supported by a wealth of experimental evidence. In EP, patch-clamp recordings demonstrate both reduced GABAergic inhibition and enhanced glutamatergic transmission, resulting in network hyperexcitability [81,82]. In AD, studies have shown that AD mouse models exhibit spontaneous epileptiform activity, while human studies using magnetoencephalography have demonstrated disruption of synchronization in multiple frequency bands [16,83].

To explore how synaptic pruning contributes to the comorbidity of AD and EP, we developed a computational model of the hippocampal CA3 circuit on top of Liu's biologically plausible EP modeling. We calibrate fixed synaptic strength by adjusting conductance-based synapses to produce realistic postsynaptic potential based on animal experiments. [16,83], while leveraging synaptic connection pruning across simulation trials on independently standard normal synaptic weights to transition the

network into abnormal states. This model allowed us to quantify how pruning of excitatory and inhibitory synapses affects E/I balance (E/I ratio) and the temporal coordination of neural firing (synchronization) [82].

Our computational model suggests that synaptic pruning can regulate the E/I balance in neural networks, with inhibitory synapse pruning having a more pronounced effect. Quantitative analysis by linear regression also suggests that excitatory synapse elimination decreased the E/I ratio (β = -1.038), while inhibitory synapse removal led to a larger increase in the E/I ratio (β = 1.454) (**Fig. 7**). Our finding that inhibitory pruning has a stronger (enhancing) effect on network dynamics can be explained by the function of inhibitory interneurons within neural circuits. These neurons often establish synaptic connections with multiple excitatory neurons and act as regulators of circuit coordination and synchronization [84]. Therefore, when inhibitory control mechanisms are impaired, the resulting disruption of regulation will trigger dysregulation that extends to more widespread circuits. Moreover, endogenous homeostatic mechanisms such as synaptic scaling appear to have a limited capacity to compensate for the loss of inhibitory synapses [85]. Ultimately, a reduction in inhibitory synapses may produce a larger perturbation in neural networks than an equivalent reduction in excitatory synapses.

Interestingly, our findings reveal a weaker correlation of synaptic pruning on network

synchronization compared to its impact on the E/I ratio. Specifically, inhibitory pruning exhibited a moderate positive correlation with synchronization (r = 0.346), whereas excitatory pruning had a negligible correlation (r = −0.039). Notably, the E/I ratio itself demonstrated a strong correlation with synchronization levels (r = 0.491). While it seems intuitive that enhancing network excitability can enhance synchrony, the results of our analysis predict the importance of considering the specific location and functional role of pruned synapses in neural circuits [84]. For instance, in a circuit that has an inhibitory effect on the broader network, pruning inhibitory synapses that inhibit this circuit will paradoxically reduce network synchronization. This explains the indirect, nonlinear association of synaptic pruning with network synchronization (**Fig. 7B**).

.

Although it is still difficult to establish a causal relationship between synaptic pruning and this comorbidity, our simulation results suggest a potential relationship, that is, the loss of neurons or synapses in neurodegenerative diseases disrupt the E/I balance of the neural network, may thereby promote epilepsy susceptibility (**Fig. 7**). In fact, epilepsy is well known as a comorbidity of multiple neurodegenerative diseases such as Huntington's and Parkinson's disease [86–88]. Our simulations show that in the case of equal loss of excitatory or inhibitory synapses (even in the case of loss more excitatory synapses than inhibitory synapses) (**Fig. 7A**), the effect of inhibitory synapses loss can overpower the effect of excitatory synapses loss, causing a more

extensive network E/I balance disruption and promoting network synchronization (**Fig. 7B**). Similar to *Tyrobp* and *Trem2* being known risk factors for AD, Mendelian randomization studies have also indicated that *C1qa* is a risk factor for both AD and EP (**Fig. S7**) [89]. In fact, in AD, synaptic loss often precedes cognitive decline and EP, which suggests that it may be an initiating event rather than a consequence [90].

Our results highlight the role of inhibitory synaptic pruning in promoting network synchronization. Notably, several recent studies have shown that microglial synaptic pruning appear to have inhibitory pruning preference [91]. Dejanovic B et al. had shown that the *Trem2-C1q* microglial synaptic pruning pathway engulfs inhibitory synapses more than excitatory synapses in AD model, while Fan J et al. demonstrated similar preferential pruning of inhibitory synapses during recurrent seizures that exacerbate EP model pathology [91,92]. At the molecular level, *C1q* acts as an "eat me" signal, tagging synapses for microglia to eliminate [78]. While this tagging process is not synapse-type specific, microglia demonstrate selective pruning of inhibitory synapses [78,91]. Studies have shown that *C1q* blockade reduces both the frequency and severity of seizures in traumatic brain injury models [93]. However, it is also important to note that *C1q* knockout also affects synaptic elimination during development, resulting in enhanced connectivity and seizure activity [94,95]. Recently, Aloi MS et al. reported that overactivation of microglia reduced amyloid-β pathology but also caused hyperexcitability and seizures via synaptic pruning [96]. These findings suggest the

importance of managing microglial *C1q*-mediated synaptic pruning during AD pathology and aging, and further exploration and regulation of this potential preferential pruning of inhibitory synapses is warranted.

Our study has two limitations: while our analysis mined a conserved microglial synaptic pruning pathway across multiple datasets, we primarily relied on bulk RNAseq data that cannot fully capture cell subtype specificity. Although we attempted to address this limitation through computational deconvolution and validation of single-cell datasets, future studies should employ spatial transcriptomic approaches to advance understanding of the cell subtype-specific contribution to AD-EP comorbidity, for example, by tracking changes in microglial activation patterns and synaptic action in AD and EP. In addition, while our computational model provides insights into the contribution of synaptic pruning to network dynamics, it simplifies many aspects of real neural circuits, such as topology and dendritic details within neural circuits. Future models could incorporate more detailed cellular mechanisms to better reflect the progression of AD and EP comorbidity at the molecular level.

Conclusion

In this study, we integrated large-scale transcriptomic datasets from multiple AD and EP animal models, as well as human patient cohorts, to identify a shared molecular pathway that converges on microglial synaptic pruning. Specifically, we found a

highly preserved immune-related co-expression module centered on the *Tyrobp-Trem2-C1q* complement pathway. Differential gene expression and gene regulatory network analysis confirmed that this pathway is consistently upregulated in both animal models and human patients. Our computational modeling further suggests a mechanistic basis for how excessive synapses pruning tip the E/I balance toward hyperexcitation, leading to the comorbidity of AD and EP.

These findings highlight a microglial-driven, complement-mediated synaptic pruning mechanism common to AD and EP. In linking the dysregulated immune response to E/I imbalances, our work provides a unifying framework that may explain the strong bidirectional comorbidity observed clinically. More broadly, these results highlight the potential of targeting microglia–complement signaling for therapeutic interventions aimed at ameliorating seizures and slowing cognitive decline in patients with AD and EP. Future studies integrating spatial transcriptomics, advanced single-cell profiling, and in vivo manipulation of complement pathways are warranted to elucidate how microglial subtypes selectively prune synapses in AD and EP, and whether modulating this process can indeed confer disease-modifying benefits.

Abbreviations

EP	Epilepsy
AD	Alzheimer’s disease

E/I	Excitation/Inhibition
TLE	Temporal lobe epilepsy
Aβ	Amyloid-β
GEO	Gene Expression Omnibus
ENA	European Nucleotide Archive
WT	Wild-type
scRNA-Seq	Single-cell RNA sequencing
snRNA-Seq	Single-nucleus RNA sequencing
PCA	Principal Component Analysis
DEGs	Differentially expressed genes
BH	Benjamini-Hochberg
KEGG	Kyoto Encyclopedia of Genes and Genomes
GO	Gene ontology
MAD	Median absolute deviation
TOM	Topological overlap matrices
MEs	Module eigengenes
MM	Module membership
GS	Gene-genotype significance
PPI	Protein-protein interaction
FDR	False discovery rate
SVM	Support vector machine

PCs	Principal components
ES	Event synchrony
BBB	Blood-brain barrier
DAM	Disease-associated microglial
LTP	Long-term potentiation
LTD	Long-term depression
BP	Biological processes
CC	Cellular components
MF	Molecular functions
HR	Hazard ratios
CI	Confidence intervals
NCBI	National Center for Biotechnology Information

Figures and legends

Figure 1: Differential Expression and Functional Enrichment Analyses in EP and AD Model Datasets.

(A) Volcano plot showing the DEGs in the EP model dataset. The x-axis represents the log2 fold change, and the y-axis shows the -log10 adjusted p-value. The dashed lines mark the thresholds for significance (adjusted p-value < 0.05 and |log2 fold change| > 1). **(B)** Differential expression analysis of the TG model dataset. Scatter plot showing progressive DEGs identified across different ages (4, 6, and 8 months)

compared to their control and initial months. The shaded regions correspond to the different age groups, with the numbers indicating the count of EP-DEGs (numerator) and total DEGs (denominator) with a log2 fold change below 1 that marks the threshold for non-significant genes. **(C)** The plot shows the expression level of single upregulated progressive DEG *Cst7* in the J20 model over time (x-axis: Age in months; y-axis: Normalized counts), with different genotypes (J20 and WT) represented by different colors. Dashed lines represent mean paths for each age. (LRTstatistic = 43.70, log2foldchange[6-12months] = 2.73, FDR = 2.91E-5). **(D)** KEGG pathway enrichment analysis of shared DEGs between the EP and TG datasets. The bubble plot indicates the significantly enriched pathways, with bubble size representing the gene count and color indicating the significance level (-log10 adjusted p-value). **(E)** GO enrichment analysis of shared DEGs between the EP and TG model datasets. The dot plot shows the enriched biological processes (BP), cellular components (CC), and molecular functions (MF). Dot size corresponds to gene count, while color represents the significance level (-log10 adjusted p-value). Immune-related functions were prominently enriched.

Figure 2: Co-Expression Network Construction and Model-Trait Association.

(A-C) Hierarchical clustering dendrograms are presented for the EP (**A**), TG (**B**), and J20 (**C**) model datasets, with gene modules identified through dynamic tree cutting. The colors in the heatmap below each dendrogram correspond to distinct gene

modules, where the clustering of similar colors between the EP and other model datasets (TG and J20) reflects the conservation of modules across conditions. The GS is shown with darker colors indicating stronger correlations: red represents positive correlations, and blue represents negative correlations with disease genotypes (EP for panel A, TG for panel B, and J20 for panel C). Overlapping red areas in the module-trait relationships suggest that these modules may be positively correlated with both EP and AD model, as seen in the turquoise module in the TG model dataset. The DEG row shows the distribution of DEGs within the modules: red indicates DEGs, while grey indicates non-DEGs. **(D-F)** Heatmaps of the module-trait relationships in EP (**D**), TG (**E**), and J20 (**F**) model datasets. The heatmaps show the Pearson correlation coefficients between MEs and genotypes. The color scale represents the strength and direction of the correlation, with red indicating positive and blue indicating negative correlations. Modules are considered as significant association with genotype using threshold (p-value < 0.05, $|r| > 0.65$).

Figure 3: Module Preservation Analysis Across EP and AD Datasets.

(A, B) Zsummary preservation statistics of EP model modules in the TG and J20 model datasets, respectively. Each point represents an EP model module, with the y-axis displaying the Zsummary preservation statistic. A Zsummary > 10 indicates strong evidence of preservation, $2 <$ Zsummary < 10 indicates moderate evidence, and Zsummary < 2 suggests no evidence of preservation. The gray horizontal line at Z =

10 and the black horizontal line at Z = 2 serve as reference points in the plots. The module size is indicated by the x-axis, and the color represents the module color. **(C-F)** Bubble plots show the cross-tabulation of EP model modules with TG (**C**) and J20 (**D**) model modules; the cross-tabulation of EP patient (GSE63808) and EP model datasets (**E**); cross-tabulation of AD (GSE132903) and TG mouse model datasets (**F**). The color scale represents the adjusted p-value for the overlap significance, while the size of the dots corresponds to the number of overlapping genes. Larger, more significant dots indicate stronger overlaps between EP and AD modules such as the turquoise module. Only significantly overlapping with overlap count > 30 and adjusted p-value < 0.05 was colored, while those with insignificant overlap are marked in gray.

Figure 4: Identification and Network Analysis of Shared Hub Genes in EP and AD Datasets.

(**A**) Network plot illustrating the top 50 genes within the conserved turquoise module across both the EP and TG model datasets. Each node represents a gene, and edges signify gene co-expression connections (Grey for EP, blue for TG). The color of the nodes indicates gene connectivity. 17 red nodes are shared hub genes that exhibit high connectivity in both networks and are identified as DEGs under both conditions. Two shared hub genes are not shown in the figure due to their ranking in both modules: *Apobec* and *Cxcl16*. (**B**) Venn diagram depicting the overlap between hub genes identified in the EP and AD datasets and shared DEGs. 19 shared hub genes were

identified as key drivers in both conditions. (**C**) PPI network of the 14 shared hub genes constructed from 19 shared hub genes using the STRING database. The size and color of the nodes are colored by their connectivity in the PPI network. (**D**) The bubble plot showed the top GO biological process enrichment terms based on p-values for the 19 shared hub genes. (**E**) The shared gene regulatory network was inferred using the GENIE3 algorithm, showing the regulatory relationships among the shared hub genes. (**F**) Progressive upregulation of key 5 shared hub genes involved in microglial synaptic pruning across different ages in the TG mouse model. The plot shows the expression level of these genes over time (x-axis: Age in months; y-axis: Normalized counts), with different genotypes represented by different colors (WT: black, TG: teal). Dashed lines represent mean paths for each age. LRT statistics of these genes can be found in **Table S2**.

Figure 5. Expression analysis and correlation patterns of shared hub genes in AD and EP patient datasets.

(**A, B**) Violin plots showing the differential expression of shared hub genes between control and disease groups in (**A**) EP patient dataset (E-MTAB-3123) and (**B**) AD patient dataset (GSE48350). Red violins represent control groups and blue violins represent disease groups. The width of each violin indicates the density of data points, and the internal box plots show the median and interquartile ranges. The Wilcoxon p-value is shown for each comparison. (**C, D**) Correlation heatmap showing the

relationships between shared hub genes and age in the EP patient dataset (E-MTAB-3123) and AD patient dataset (GSE48350). The color intensity and box size represent the strength of Pearson correlation coefficients (r), with red indicating positive correlations and blue indicating negative correlations.

Figure 6: Cellular Composition Deconvolution and Association with Shared Hub Genes in EP and TG Datasets.

(**A, C**) The plot shows the estimated proportions of different cell types (astrocytes, neurons, oligodendrocytes, microglia, and endothelial) in control and EP model conditions (**A**), and TG model condition (**C**). The x-axis represents different conditions or months, and the y-axis shows the proportions of specific cell types in each condition, with different genotypes represented by different colors. The Mann-Whitney test was performed to determine significant cell composition difference ($p < 0.05$) in EP model dataset. The Kruskal-Wallis test was performed to determine the significance ($q < 0.05$) with the BH method was used to adjust the p-value in pairwise comparisons among different groups in the TG model dataset. (**B, D**) Correlation heatmap showing the relationships between key shared hub genes and cell composition in the EP model dataset. The color intensity represents the strength of Pearson correlation coefficients (r), with red indicating positive correlations and blue indicating negative correlations. The significance of correlations with shared hub gene is shown by red arrows, with arrow color proportional to correlation strength.

Figure 7. Effects of excitatory and inhibitory synaptic pruning on neural network dynamics.

(**A**) Four-dimensional plot showing the simulation results of excitatory pruning ratio (0-0.5), inhibitory pruning ratio (0-0.5), E/I ratio, and synchronization. The surface visualizes the variation of the average E/I ratio with different pruning condition. Colors indicate average synchronization levels from dark purple (close to 1, indicating no change in synchrony) to yellow (indicating higher synchrony). (**B**) Correlation plot showing the relationships among synapse pruning, E/I ratio and synchronization. The color intensity represents the strength of Pearson correlation coefficients (r), with red indicating positive correlations and blue indicating negative correlations.

Legends of supplementary files

Table S1: Summary of Quality Control and Mapping Statistics for Bulk RNA-seq Samples.

Detailed summary of the QC and mapping statistics for all RNA-seq samples analyzed in this study. For each sample, the total number of raw reads, the number of reads passing quality filtering through Fastp, and the reads retained after rRNA contamination removal by ribodetector are reported. Each sample is categorized by the experimental group, including relevant age and condition tags, and further

classified into either the AD or EP dataset. Notes regarding any specific issues or annotations on individual samples are also provided.

Table S2: Differential Expression and Functional Enrichment Analysis of Shared DEGs.

Summary of differential expression and functional enrichment analyses across three datasets: EP, TG, and J20 mouse models.

Table S3: Module Construction, Preservation, and Functional Enrichment of Gene Co-Expression Networks in Mouse Models.

Summary of WGCNA on EP, TG, and J20 mouse models. The table is divided into multiple sections, including the gene modules' membership identified in each dataset and their correlations with model-specific genotypes. Additionally, module preservation analyses between the EP and AD datasets are included. GO enrichment analyses of the turquoise modules are also shown.

Table S4: Protein-Protein Interaction Network and GO Biological Process Enrichment Analysis of Shared Hub Genes.

Analysis results of the PPI network constructed for 19 shared hub genes identified across EP and TG models. The table is divided into three sections. The PPI GO sheet summarizes the results of the GO biological process enrichment analysis. The PPI

Degree sheet lists each gene and its degree of connectivity within the network. The PPI Interaction sheet details the specific interactions between these genes.

Table S5: Regulatory Network Prediction Using GENIE3 for Turquoise Module in Mice Models.

Results of regulatory network inference were conducted using the GENIE3 machine learning algorithm on the gene expression profiles of the turquoise module from the EP and TG models. The table is divided into two sections: GENIE3TG and GENIE3EP, representing the predicted regulatory relationships within the TG and EP datasets, respectively. Each section lists the regulatory gene, the target gene, and the corresponding weight of the predicted regulatory interaction.

Table S6: Cell Composition Deconvolution of Bulk RNA-seq Data.

Results of cell composition deconvolution analysis conducted using CIBERSORT from BrainDeconvShiny on bulk RNA-seq data from the EP and AD models. The table includes the estimated proportions of major brain cell types, including neurons, astrocytes, oligodendrocytes, microglia, and endothelial for each sample, alongside the sample identifiers, group classification, age, and condition type (e.g., rTg4510, Wild Type).

Figure S1. Construction of co-expression module in model datasets.

(**A-C**) Hierarchical clustering dendrograms and trait heatmaps for the EP, rTg4510, and J20 datasets. (**A**) EP dataset, (**B**) rTg4510 dataset, and (**C)** J20 dataset. Hierarchical clustering was performed on variance-stabilized gene expression data to identify potential outliers. The top 85% of genes with the highest Median Absolute Deviation (MAD) were retained, and outliers were detected and removed before network construction. Two samples were removed from the rTg4510 dataset, and three samples were removed from the J20 dataset. The heatmaps below each dendrogram display the trait data associated with each sample, with red indicating outliers or specific traits of interest. **(D-E)** Soft-thresholding power Selection and Comparability Assessment, **(D)** Selection of the soft-thresholding power for network construction. The left panel shows the scale-free topology fit index (y-axis) as a function of the soft-thresholding power (x-axis) for EP, TG, and J20 datasets. The right panel depicts the mean connectivity (y-axis) against soft-thresholding power, indicating that a power of 9 was chosen for all datasets to achieve scale-free topology with $R^2 > 0.85$. **(E)** Comparability assessment of the EP, TG, and J20 datasets. Scatter plots display the correlations between ranked mean gene expression (top) and ranked gene connectivity (bottom) between EP and TG datasets (left) and between EP and J20 datasets (right). Positive correlations and significant P values suggest strong comparability between datasets.

Figure S2. Construction of co-expression module in patient datasets.

(**A**) Scale independence and mean connectivity plots across soft-thresholding powers for the EP (GSE63808) and AD (GSE132903) patient datasets, with a selected soft-thresholding power of 9 ensuring a scale-free topology (R^2 ≥ 0.85). (**B-C**) Dendrogram of gene modules identified in the EP and AD dataset using hierarchical clustering and dynamic tree cutting based on topological overlap matrices (TOM).

Figure S3: ROC curve of Diagnostic model.

(**A**) in EP patient dataset (E-MTAB-3123) and (**B**) in AD patient dataset (GSE48350). ROC curves of various machine learning classifiers in classifying disease cases from control participants based on selected gene expression data. Remarkably, most of the models have an AUC between 0.85 and 0.92 in EP patient dataset, with the best performance recorded with XGBoost, reaching the highest AUC score in this EP dataset (AUC = 0.92). Although the AD model diagnostic efficiency is not as high as that of the EP dataset, which may reflect the complex disease background of AD, these diagnostic models still show high diagnostic efficiency (AUC > 0.7).

Figure S4: Cellular Composition Deconvolution and Association with Shared Hub Genes in J20 Datasets.

(**A**) The plot shows the cell composition level over time in J20 dataset (x-axis: Age in months; y-axis: Normalized counts), with different genotypes represented by different colors (WT: black, J20: teal). Dashed lines represent mean paths for each age. The

Kruskal-Wallis test was performed to determine the significance with the BH method was used to adjust the p-value in pairwise comparisons among different groups, with a significance level of $q < 0.05$. (**B**) Correlation heatmap showing the relationships between key shared hub genes and cell composition in the J20 model dataset. The color intensity represents the strength of Pearson correlation coefficients (r), with red indicating positive correlations and blue indicating negative correlations.

Figure S5: Expression Localization of Shared Hub Genes in Mouse Brain Cell Types.

This figure shows the expression patterns of 19 shared hub genes across various cell types in the mouse brain, based on the Whole Mouse Brain Transcriptomic Cell Type Atlas (https://assets.nemoarchive.org/dat-qg7n1b0) from the Allen Brain Cell Atlas. The top left panel illustrates the localization and color of various cell types, such as astrocytes, microglia, macrophages, endothelial cells, and oligodendrocytes in the brain atlas. Each circular panel highlights the specific expression profile of one gene, with darker shading representing higher expression levels. Most of these genes (15 out of 19) are predominantly expressed in immune cells, specifically microglia and macrophages.

Figure S6: sc/nRNAseq Analysis of Shared Hub Gene Expression in Immune Cells of Patients.

(**A, D**) Dot plot displaying the expression of shared hub genes across different identified cell types in the EP patient dataset. The size of the dots represents the proportion of cells expressing each gene, and the color intensity indicates the average expression level. (**A**) EP patient dataset (GSE227223), (**D**) AD patient dataset (GSE201048). (**B, E**) t-SNE plot showing the clustering of cells in the EP and AD dataset based on their gene expression profiles, with distinct colors representing different cell types. (**B**) EP dataset, (**E**) AD dataset. (**C, F**) Feature plots showing the expression patterns of individual hub genes within the EP dataset, over on the t-SNE map. Darker purple areas represent higher expression levels. *TYROBP*, *TREM2*, *C1QA*, *C1QB*, and *C1QC* exhibit high expression predominantly in microglia clusters. (C) EP dataset, (F) AD dataset.

Figure S7: Forest plot of Mendelian randomization result from DMRdb.

Forest plot showing hazard ratios (HR) and 95% confidence intervals (CI) for associations between Alzheimer's disease subtypes, epilepsy, and *C1QA* http://www.inbirg.com/DMRdb/. Red dots represent point estimates for hazard ratios, and horizontal lines indicate 95% confidence intervals. p-values are shown for each association. Values greater than 1.0 indicate increased risk for the outcome.

Declarations

Ethics approval and consent to participate

Not applicable.

Consent for publication

Not applicable.

Availability of data and materials

The datasets analyzed during the current study are available in the National Center for Biotechnology Information (NCBI) or European Nucleotide Archive (ENA) under the following accession numbers: PRJEB18790, GSE125957, GSE48350, E-MTAB-3123, GSE63808, GSE132903, GSE201048, and GSE227223.

Competing Interests

The authors declare that they have no known competing financial interests or personal relationships that could have appeared to influence the work reported in this paper.

Funding

This research was supported by the Young Scientists Fund of the National Natural Science Foundation of China (Grant Nos. 82201629) and the Guangdong Provincial Science and Technology Special Fund (Grant Nos. 210803136872196)

Authors' contribution

HL conceptualized the study, conducted the investigation, developed the methodology, performed formal analysis, and contributed to writing the original draft and reviewing/editing the manuscript. ZX, YT, and BL contributed to the investigation, performed formal analysis, and participated in writing the original draft and reviewing/editing the manuscript. JL contributed to writing the original draft and reviewing/editing the manuscript. JW was involved in conceptualization and contributed to writing the original draft and reviewing/editing the manuscript. MC, XL, YS, SC, ZD, and MH contributed to the investigation and participated in reviewing/editing the manuscript. BH and NW conceptualized the study and contributed to writing the original draft and reviewing/editing the manuscript. XJ provided supervision, acquired funding, contributed to conceptualization, and participated in writing the original draft and reviewing/editing the manuscript. All authors read and approved the final manuscript.

Acknowledgments

Not applicable

References

1. Giorgi FS, Saccaro LF, Busceti CL, Biagioni F, Fornai F. Epilepsy and Alzheimer's Disease: Potential mechanisms for an association. Brain Research Bulletin. 2020 Jul 1;160:107-20.
2. Kamondi A, Grigg-Damberger M, Löscher W, Tanila H, Horvath AA. Epilepsy and epileptiform activity in late-onset Alzheimer disease: Clinical and pathophysiological advances, gaps and conundrums. Nature Reviews Neurology. 2024 Mar;20(3):162-82.
3. Fang Y, Si X, Wang J, Wang Z, Chen Y, Liu Y, Yan Y, Tian J, Zhang B, Pu J. Alzheimer disease and epilepsy: A Mendelian randomization study. Neurology. 2023 Jul 25;101(4):e399-409.
4. Wimo A, Jönsson L, Bond J, Prince M, Winblad B, International AD. The worldwide economic impact of dementia 2010. Alzheimer's & dementia. 2013 Jan 1;9(1):1-1.
5. Ngugi AK, Bottomley C, Kleinschmidt I, Sander JW, Newton CR. Estimation of the burden of active and life□time epilepsy: a meta□analytic approach. Epilepsia. 2010 May;51(5):883-90.
6. Mendez MF, Lim GT. Seizures in elderly patients with dementia: epidemiology and management. Drugs & aging. 2003 Sep;20:791-803.
7. Leitner D, Pires G, Kavanagh T, Kanshin E, Askenazi M, Ueberheide B, Devinsky O, Wisniewski T, Drummond E. Similar brain proteomic signatures in Alzheimer's disease and epilepsy. Acta Neuropathologica. 2024 Jun;147(1):27.
8. Pandis D, Scarmeas N. Seizures in alzheimer disease: clinical and epidemiological data: Seizures in alzheimer disease. Epilepsy currents. 2012 Sep;12(5):184-7.
9. Tombini M, Assenza G, Ricci L, Lanzone J, Boscarino M, Vico C, Magliozzi A, Di Lazzaro V. Temporal lobe epilepsy and Alzheimer's disease: from preclinical to clinical evidence of a strong association. Journal of Alzheimer's disease reports. 2021 Jan 1;5(1):243-61.
10. Johnson EL, Krauss GL, Lee AK, Schneider AL, Dearborn JL, Kucharska-Newton AM, Huang J, Alonso A, Gottesman RF. Association between midlife risk factors and late-onset epilepsy: results from the atherosclerosis risk in communities study. JAMA neurology. 2018 Nov 1;75(11):1375-82.
11. Stefanidou M, Beiser AS, Himali JJ, Peng TJ, Devinsky O, Seshadri S, Friedman D. Bi-directional association between epilepsy and dementia: The Framingham Heart Study. Neurology. 2020 Dec 15;95(24):e3241-7.
12. Gourmaud S, Shou H, Irwin DJ, Sansalone K, Jacobs LM, Lucas TH, Marsh ED, Davis KA, Jensen FE, Talos DM. Alzheimer-like amyloid and tau alterations associated with cognitive deficit in temporal lobe epilepsy. Brain. 2020 Jan 1;143(1):191-209.
13. Tai XY, Koepp M, Duncan JS, Fox N, Thompson P, Baxendale S, Liu JY,

Reeves C, Michalak Z, Thom M. Hyperphosphorylated tau in patients with refractory epilepsy correlates with cognitive decline: a study of temporal lobe resections. Brain. 2016 Sep 1;139(9):2441-55.

14. Zou Y, Wang C, Li H, Zhong M, Lin J, Hu Y, Chen Z, Gan CL. Epileptic seizures induced by pentylenetetrazole kindling accelerate Alzheimer-like neuropathology in 5× FAD mice. Frontiers in Pharmacology. 2024 Oct 31;15:1500105.
15. Watts ME, Pocock R, Claudianos C. Brain energy and oxygen metabolism: emerging role in normal function and disease. Frontiers in molecular neuroscience. 2018 Jun 22;11:216.
16. Born HA. Seizures in Alzheimer’s disease. Neuroscience. 2015 Feb 12;286:251-63.
17. Toniolo S, Sen A, Husain M. Modulation of brain hyperexcitability: potential new therapeutic approaches in Alzheimer’s disease. International journal of molecular sciences. 2020 Dec 7;21(23):9318.
18. Liew Y, Retinasamy T, Arulsamy A, Ali I, Jones NC, O’Brien TJ, Shaikh MF. Neuroinflammation: A common pathway in Alzheimer’s disease and epilepsy. Journal of Alzheimer's Disease. 2023 Jan 1;94(s1):S253-65.
19. Kalyvas AC, Dimitriou M, Ioannidis P, Grigoriadis N, Afrantou T. Alzheimer’s Disease and Epilepsy: Exploring Shared Pathways and Promising Biomarkers for Future Treatments. Journal of Clinical Medicine. 2024 Jan;13(13):3879.
20. Targa Dias Anastacio H, Matosin N, Ooi L. Neuronal hyperexcitability in Alzheimer’s disease: what are the drivers behind this aberrant phenotype?. Translational psychiatry. 2022 Jun 22;12(1):257.
21. Tang Y, Yan Y, Mao J, Ni J, Qing H. The hippocampus associated GABAergic neural network impairment in early-stage of Alzheimer's disease. Ageing Research Reviews. 2023 Apr 1;86:101865.
22. Bosco F, Guarnieri L, Rania V, Palma E, Citraro R, Corasaniti MT, Leo A, De Sarro G. Antiseizure medications in Alzheimer’s disease from preclinical to clinical evidence. International journal of molecular sciences. 2023 Aug 10;24(16):12639.
23. Andrews S, Krueger F, Segonds-Pichon A, Biggins L, Kruger C, Wingett S. FastQC. Babraham Bioinformatics. Cambridge, UK. 2010.
24. Chen S, Zhou Y, Chen Y, Gu J. fastp: an ultra-fast all-in-one FASTQ preprocessor. Bioinformatics. 2018 Sep 1;34(17):i884-90.
25. Deng ZL, Münch PC, Mreches R, McHardy AC. Rapid and accurate identification of ribosomal RNA sequences via deep learning. Nucleic acids research. 2022 Jun 10;50(10):e60-.
26. Kim D, Paggi JM, Park C, Bennett C, Salzberg SL. Graph-based genome alignment and genotyping with HISAT2 and HISAT-genotype. Nature biotechnology. 2019 Aug;37(8):907-15.

27. Liao Y, Smyth GK, Shi W. featureCounts: an efficient general purpose program for assigning sequence reads to genomic features. Bioinformatics. 2014 Apr 1;30(7):923-30.
28. Love MI, Huber W, Anders S. Moderated estimation of fold change and dispersion for RNA-seq data with DESeq2. Genome biology. 2014 Dec;15:1-21.
29. Castanho I, Murray TK, Hannon E, Jeffries A, Walker E, Laing E, Baulf H, Harvey J, Bradshaw L, Randall A, Moore K. Transcriptional signatures of tau and amyloid neuropathology. Cell Reports. 2020 Feb 11;30(6):2040-54.
30. Elizarraras JM, Liao Y, Shi Z, Zhu Q, Pico AR, Zhang B. WebGestalt 2024: faster gene set analysis and new support for metabolomics and multi-omics. Nucleic Acids Research. 2024 May 29:gkae456.
31. Miller JA, Horvath S, Geschwind DH. Divergence of human and mouse brain transcriptome highlights Alzheimer disease pathways. Proceedings of the National Academy of Sciences. 2010 Jul 13;107(28):12698-703.
32. Langfelder P, Horvath S. WGCNA: an R package for weighted correlation network analysis. BMC bioinformatics. 2008 Dec;9:1-3.
33. Zhang B, Horvath S. A general framework for weighted gene co-expression network analysis. Statistical applications in genetics and molecular biology. 2005 Aug 12;4(1).
34. Ritchie ME, Phipson B, Wu DI, Hu Y, Law CW, Shi W, Smyth GK. limma powers differential expression analyses for RNA-sequencing and microarray studies. Nucleic acids research. 2015 Apr 20;43(7):e47-.
35. Schober P, Boer C, Schwarte LA. Correlation coefficients: appropriate use and interpretation. Anesthesia & analgesia. 2018 May 1;126(5):1763-8.
36. Langfelder P, Luo R, Oldham MC, Horvath S. Is my network module preserved and reproducible?. PLoS computational biology. 2011 Jan 20;7(1):e1001057.
37. Szklarczyk D, Kirsch R, Koutrouli M, Nastou K, Mehryary F, Hachilif R, Gable AL, Fang T, Doncheva NT, Pyysalo S, Bork P. The STRING database in 2023: protein–protein association networks and functional enrichment analyses for any sequenced genome of interest. Nucleic acids research. 2023 Jan 6;51(D1):D638-46.
38. Huynh-Thu VA, Irrthum A, Wehenkel L, Geurts P. Inferring regulatory networks from expression data using tree-based methods. PloS one. 2010 Sep 28;5(9):e12776.
39. Newman AM, Liu CL, Green MR, Gentles AJ, Feng W, Xu Y, Hoang CD, Diehn M, Alizadeh AA. Robust enumeration of cell subsets from tissue expression profiles. Nature methods. 2015 May;12(5):453-7.
40. Sutton GJ, Poppe D, Simmons RK, Walsh K, Nawaz U, Lister R,

Gagnon-Bartsch JA, Voineagu I. Comprehensive evaluation of deconvolution methods for human brain gene expression. Nature Communications. 2022 Mar 15;13(1):1358.

41. Robinson MD, McCarthy DJ, Smyth GK. edgeR: a Bioconductor package for differential expression analysis of digital gene expression data. bioinformatics. 2010 Jan 1;26(1):139-40.

42. Zhang Y, Chen K, Sloan SA, Bennett ML, Scholze AR, O'Keeffe S, Phatnani HP, Guarnieri P, Caneda C, Ruderisch N, Deng S. An RNA-sequencing transcriptome and splicing database of glia, neurons, and vascular cells of the cerebral cortex. Journal of neuroscience. 2014 Sep 3;34(36):11929-47.

43. Hao Y, Stuart T, Kowalski MH, Choudhary S, Hoffman P, Hartman A, Srivastava A, Molla G, Madad S, Fernandez-Granda C, Satija R. Dictionary learning for integrative, multimodal and scalable single-cell analysis. Nature biotechnology. 2024 Feb;42(2):293-304.

44. Kumar P, Lim A, Hazirah SN, Chua CJ, Ngoh A, Poh SL, Yeo TH, Lim J, Ling S, Sutamam NB, Petretto E. Single-cell transcriptomics and surface epitope detection in human brain epileptic lesions identifies pro-inflammatory signaling. Nature Neuroscience. 2022 Jul;25(7):956-66.

45. Sun N, Victor MB, Park YP, Xiong X, Scannail AN, Leary N, Prosper S, Viswanathan S, Luna X, Boix CA, James BT. Human microglial state dynamics in Alzheimer’s disease progression. Cell. 2023 Sep 28;186(20):4386-403.

46. Stimberg M, Brette R, Goodman DF. Brian 2, an intuitive and efficient neural simulator. elife. 2019 Aug 20;8:e47314.

47. Izhikevich EM. Simple model of spiking neurons. IEEE Transactions on neural networks. 2003 Nov;14(6):1569-72.

48. Tzavellas NP, Tsamis KI, Katsenos AP, Davri AS, Simos YV, Nikas IP, Bellos S, Lekkas P, Kanellos FS, Konitsiotis S, Labrakakis C. Firing Alterations of Neurons in Alzheimer’s Disease: Are They Merely a Consequence of Pathogenesis or a Pivotal Component of Disease Progression?. Cells. 2024 Feb 29;13(5):434.

49. Sammons RP, Vezir M, Moreno-Velasquez L, Cano G, Orlando M, Sievers M, Grasso E, Metodieva VD, Kempter R, Schmidt H, Schmitz D. Structure and function of the hippocampal CA3 module. Proceedings of the National Academy of Sciences. 2024 Feb 6;121(6):e2312281120.

50. Vyleta NP, Borges-Merjane C, Jonas P. Plasticity-dependent, full detonation at hippocampal mossy fiber–CA3 pyramidal neuron synapses. Elife. 2016 Oct 25;5:e17977.

51. Liu Y, Grigorovsky V, Bardakjian B. Excitation and inhibition balance underlying epileptiform activity. IEEE Transactions on Biomedical

Engineering. 2020 Jan 1;67(9):2473-81.
52. Penn Y, Segal M, Moses E. Network synchronization in hippocampal neurons. Proceedings of the National Academy of Sciences. 2016 Mar 22;113(12):3341-6.
53. Yao Z, van Velthoven CT, Kunst M, Zhang M, McMillen D, Lee C, Jung W, Goldy J, Abdelhak A, Aitken M, Baker K. A high-resolution transcriptomic and spatial atlas of cell types in the whole mouse brain. Nature. 2023 Dec 14;624(7991):317-32.
54. Vezzani A, French J, Bartfai T, Baram TZ. The role of inflammation in epilepsy. Nature reviews neurology. 2011 Jan;7(1):31-40.
55. Heneka MT, Golenbock DT, Latz E. Innate immunity in Alzheimer's disease. Nature immunology. 2015 Mar;16(3):229-36.
56. Pekny M, Pekna M. Astrocyte reactivity and reactive astrogliosis: costs and benefits. Physiological reviews. 2014 Oct;94(4):1077-98.
57. Chen ZP, Wang S, Zhao X, Fang W, Wang Z, Ye H, Wang MJ, Ke L, Huang T, Lv P, Jiang X. Lipid-accumulated reactive astrocytes promote disease progression in epilepsy. Nature neuroscience. 2023 Apr;26(4):542-54.
58. Onyango IG, Jauregui GV, Čarná M, Bennett Jr JP, Stokin GB. Neuroinflammation in Alzheimer’s disease. Biomedicines. 2021 May 7;9(5):524.
59. Vezzani A, Viviani B. Neuromodulatory properties of inflammatory cytokines and their impact on neuronal excitability. Neuropharmacology. 2015 Sep 1;96:70-82.
60. Van Vliet EA, Aronica E, Gorter JA. Blood–brain barrier dysfunction, seizures and epilepsy. InSeminars in cell & Developmental biology 2015 Feb 1 (Vol. 38, pp. 26-34). Academic Press.
61. Zlokovic BV. Neurovascular pathways to neurodegeneration in Alzheimer's disease and other disorders. Nature Reviews Neuroscience. 2011 Dec;12(12):723-38.
62. Kopczynska M, Zelek WM, Vespa S, Touchard S, Wardle M, Loveless S, Thomas RH, Hamandi K, Morgan BP. Complement system biomarkers in epilepsy. Seizure. 2018 Aug 1;60:1-7.
63. Veerhuis R, Nielsen HM, Tenner AJ. Complement in the brain. Molecular immunology. 2011 Aug 1;48(14):1592-603.
64. Haure-Mirande JV, Audrain M, Ehrlich ME, Gandy S. Microglial TYROBP/DAP12 in Alzheimer’s disease: Transduction of physiological and pathological signals across TREM2. Molecular neurodegeneration. 2022 Aug 24;17(1):55.
65. Pottier C, Ravenscroft TA, Brown PH, Finch NA, Baker M, Parsons M, Asmann YW, Ren Y, Christopher E, Levitch D, van Blitterswijk M. TYROBP genetic variants in early-onset Alzheimer's disease.

Neurobiology of aging. 2016 Dec 1;48:222-e9.
66. Neumann H, Daly MJ. Variant TREM2 as risk factor for Alzheimer's disease. N Engl J Med. 2013 Jan 10;368(2):182-4.
67. Stevens B, Allen NJ, Vazquez LE, Howell GR, Christopherson KS, Nouri N, Micheva KD, Mehalow AK, Huberman AD, Stafford B, Sher A. The classical complement cascade mediates CNS synapse elimination. Cell. 2007 Dec 14;131(6):1164-78.
68. Paolicelli RC, Ferretti MT. Function and dysfunction of microglia during brain development: consequences for synapses and neural circuits. Frontiers in Synaptic Neuroscience. 2017 May 10;9:9.
69. Audrain M, Haure-Mirande JV, Wang M, Kim SH, Fanutza T, Chakrabarty P, Fraser P, St George-Hyslop PH, Golde TE, Blitzer RD, Schadt EE. Integrative approach to sporadic Alzheimer's disease: deficiency of TYROBP in a tauopathy mouse model reduces C1q and normalizes clinical phenotype while increasing spread and state of phosphorylation of tau. Molecular psychiatry. 2019 Sep;24(9):1383-97.
70. Haure-Mirande JV, Audrain M, Fanutza T, Kim SH, Klein WL, Glabe C, Readhead B, Dudley JT, Blitzer RD, Wang M, Zhang B. Deficiency of TYROBP, an adapter protein for TREM2 and CR3 receptors, is neuroprotective in a mouse model of early Alzheimer's pathology. Acta neuropathologica. 2017 Nov;134:769-88.
71. Haure-Mirande JV, Wang M, Audrain M, Fanutza T, Kim SH, Heja S, Readhead B, Dudley JT, Blitzer RD, Schadt EE, Zhang B. Integrative approach to sporadic Alzheimer's disease: deficiency of TYROBP in cerebral Aβ amyloidosis mouse normalizes clinical phenotype and complement subnetwork molecular pathology without reducing Aβ burden. Molecular psychiatry. 2019 Mar;24(3):431-46.
72. Neniskyte U, Gross CT. Errant gardeners: glial-cell-dependent synaptic pruning and neurodevelopmental disorders. Nature Reviews Neuroscience. 2017 Nov;18(11):658-70.
73. Hu Y, Qi H, Yang J, Wang F, Peng X, Chen X, Zhu X. Wogonin mitigates microglia-mediated synaptic over-pruning and cognitive impairment following epilepsy. Phytomedicine. 2024 Dec 1;135:156222.
74. Wu X, Gao Y, Shi C, Tong J, Ma D, Shen J, Yang J, Ji M. Complement C1q drives microglia-dependent synaptic loss and cognitive impairments in a mouse model of lipopolysaccharide-induced neuroinflammation. Neuropharmacology. 2023 Oct 1;237:109646.
75. Bie B, Wu J, Foss JF, Naguib M. Activation of mGluR1 mediates C1q-dependent microglial phagocytosis of glutamatergic synapses in Alzheimer's rodent models. Molecular neurobiology. 2019 Aug 15;56:5568-85.
76. Wu J, Bie B, Foss JF, Naguib M. Amyloid fibril–induced astrocytic

glutamate transporter disruption contributes to complement C1q-mediated microglial pruning of glutamatergic synapses. Molecular Neurobiology. 2020 May;57:2290-300.

77. Iweka CA, Seigneur E, Hernandez AL, Paredes SH, Cabrera M, Blacher E, Pasternak CT, Longo FM, de Lecea L, Andreasson KI. Myeloid deficiency of the intrinsic clock protein BMAL1 accelerates cognitive aging by disrupting microglial synaptic pruning. Journal of Neuroinflammation. 2023 Feb 24;20(1):48.

78. Andoh M, Ikegaya Y, Koyama R. Synaptic pruning by microglia in epilepsy. Journal of clinical medicine. 2019 Dec 9;8(12):2170.

79. Yuan P, Zhang M, Tong L, Morse TM, McDougal RA, Ding H, Chan D, Cai Y, Grutzendler J. PLD3 affects axonal spheroids and network defects in Alzheimer's disease. Nature. 2022 Dec 8;612(7939):328-37.

80. Stefanescu RA, Shivakeshavan RG, Talathi SS. Computational models of epilepsy. Seizure. 2012 Dec 1;21(10):748-59.

81. Fritschy JM. Epilepsy, E/I balance and GABAA receptor plasticity. Frontiers in molecular neuroscience. 2008 Mar 28;1:201.

82. Ren X, Brodovskaya A, Hudson JL, Kapur J. Connectivity and neuronal synchrony during seizures. Journal of Neuroscience. 2021 Sep 8;41(36):7623-35.

83. van Nifterick AM, de Haan W, Stam CJ, Hillebrand A, Scheltens P, van Kesteren RE, Gouw AA. Functional network disruption in cognitively unimpaired autosomal dominant Alzheimer's disease: a magnetoencephalography study. Brain Communications. 2024;6(6):fcae423.

84. Luo L. Architectures of neuronal circuits. Science. 2021 Sep 3;373(6559):eabg7285.

85. Dzyubenko E, Fleischer M, Manrique-Castano D, Borbor M, Kleinschnitz C, Faissner A, Hermann DM. Inhibitory control in neuronal networks relies on the extracellular matrix integrity. Cellular and Molecular Life Sciences. 2021 Jul;78:5647-63.

86. Neri S, Mastroianni G, Gardella E, Aguglia U, Rubboli G. Epilepsy in neurodegenerative diseases. Epileptic Disorders. 2022 Apr;24(2):249-73.

87. Cano A, Fonseca E, Ettcheto M, Sánchez-López E, de Rojas I, Alonso-Lana S, Morato X, Souto EB, Toledo M, Boada M, Marquie M. Epilepsy in neurodegenerative diseases: related drugs and molecular pathways. Pharmaceuticals. 2021 Oct 18;14(10):1057.

88. Paudel YN, Angelopoulou E, Piperi C, Othman I, Shaikh MF. Revisiting the impact of neurodegenerative proteins in epilepsy: focus on alpha-synuclein, beta-amyloid, and tau. Biology. 2020 Jun 12;9(6):122.

89. Zheng X, Tian Z, Che X, Zhang X, Xiang Y, Ge Z, Zhai Z, Ma Q, Pan J. DMRdb: a disease-centric Mendelian randomization database for

systematically assessing causal relationships of diseases with genes, proteins, CpG sites, metabolites and other diseases. Nucleic Acids Research. 2025 Jan 6;53(D1):D1363-71.

90. Chin J, Scharfman HE. Shared cognitive and behavioral impairments in epilepsy and Alzheimer's disease and potential underlying mechanisms. Epilepsy & Behavior. 2013 Mar 1;26(3):343-51.

91. Dejanovic B, Wu T, Tsai MC, Graykowski D, Gandham VD, Rose CM, Bakalarski CE, Ngu H, Wang Y, Pandey S, Rezzonico MG. Complement C1q-dependent excitatory and inhibitory synapse elimination by astrocytes and microglia in Alzheimer’s disease mouse models. Nature Aging. 2022 Sep;2(9):837-50.

92. Fan J, Dong X, Tang Y, Wang X, Lin D, Gong L, Chen C, Jiang J, Shen W, Xu A, Zhang X. Preferential pruning of inhibitory synapses by microglia contributes to alteration of the balance between excitatory and inhibitory synapses in the hippocampus in temporal lobe epilepsy. CNS Neuroscience & Therapeutics. 2023 Oct;29(10):2884-900.

93. Holden SS, Grandi FC, Aboubakr O, Higashikubo B, Cho FS, Chang AH, Forero AO, Morningstar AR, Mathur V, Kuhn LJ, Suri P. Complement factor C1q mediates sleep spindle loss and epileptic spikes after mild brain injury. Science. 2021 Sep 10;373(6560):eabj2685.

94. Chu Y, Jin X, Parada I, Pesic A, Stevens B, Barres B, Prince DA. Enhanced synaptic connectivity and epilepsy in C1q knockout mice. Proceedings of the National Academy of Sciences. 2010 Apr 27;107(17):7975-80.

95. Ma Y, Ramachandran A, Ford N, Parada I, Prince DA. Remodeling of dendrites and spines in the C1q knockout model of genetic epilepsy. Epilepsia. 2013 Jul;54(7):1232-9.

96. Aloi MS, Prater KE, Sánchez RE, Beck A, Pathan JL, Davidson S, Wilson A, Keene CD, De La Iglesia H, Jayadev S, Garden GA. Microglia specific deletion of miR-155 in Alzheimer’s disease mouse models reduces amyloid-β pathology but causes hyperexcitability and seizures. Journal of neuroinflammation. 2023 Mar 7;20(1):60.

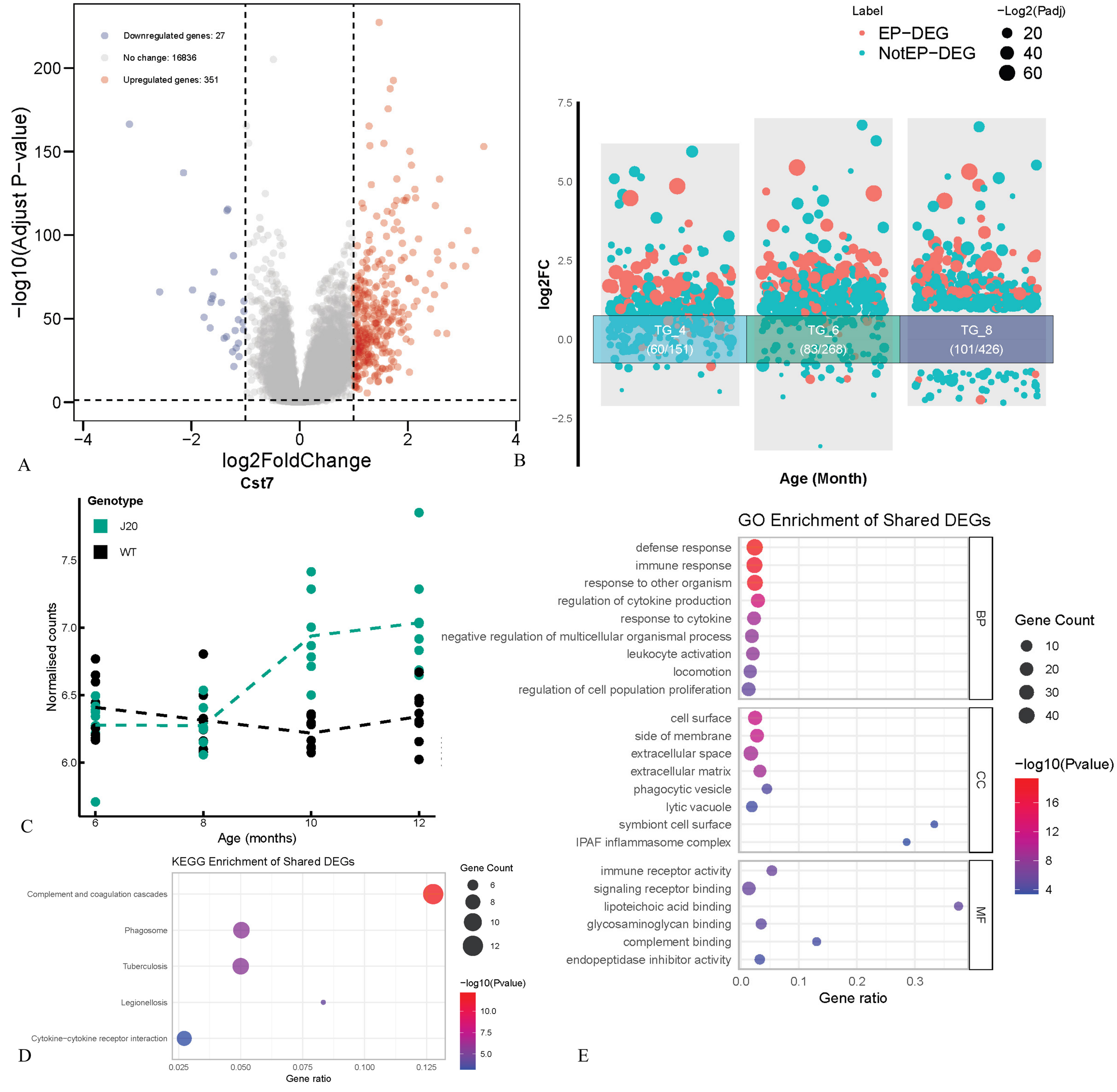
Downregulated genes: 27
No change: 16836
Upregulated genes: 351
−log10(Adjust P−value)
log2FoldChange
A
Label
EP−DEG
NotEP−DEG
−Log2(Padj)
20
40
60
log2FC
TG_4
(60/151)
TG_6
(83/268)
TG_8
(101/426)
Age (Month)
B
Genotype
J20
WT
Normalised counts
Age (months)
C
KEGG Enrichment of Shared DEGs
Complement and coagulation cascades
Phagosome
Tuberculosis
Legionellosis
Cytokine−cytokine receptor interaction
Gene ratio
Gene Count
−log10(Pvalue)
D
GO Enrichment of Shared DEGs
defense response
immune response
response to other organism
regulation of cytokine production
response to cytokine
negative regulation of multicellular organismal process
leukocyte activation
locomotion
regulation of cell population proliferation
BP
cell surface
side of membrane
extracellular space
extracellular matrix
phagocytic vesicle
lytic vacuole
symbiont cell surface
IPAF inflammasome complex
CC
immune receptor activity
signaling receptor binding
lipoteichoic acid binding
glycosaminoglycan binding
complement binding
endopeptidase inhibitor activity
MF
Gene ratio
Gene Count
−log10(Pvalue)
E

Figure 1

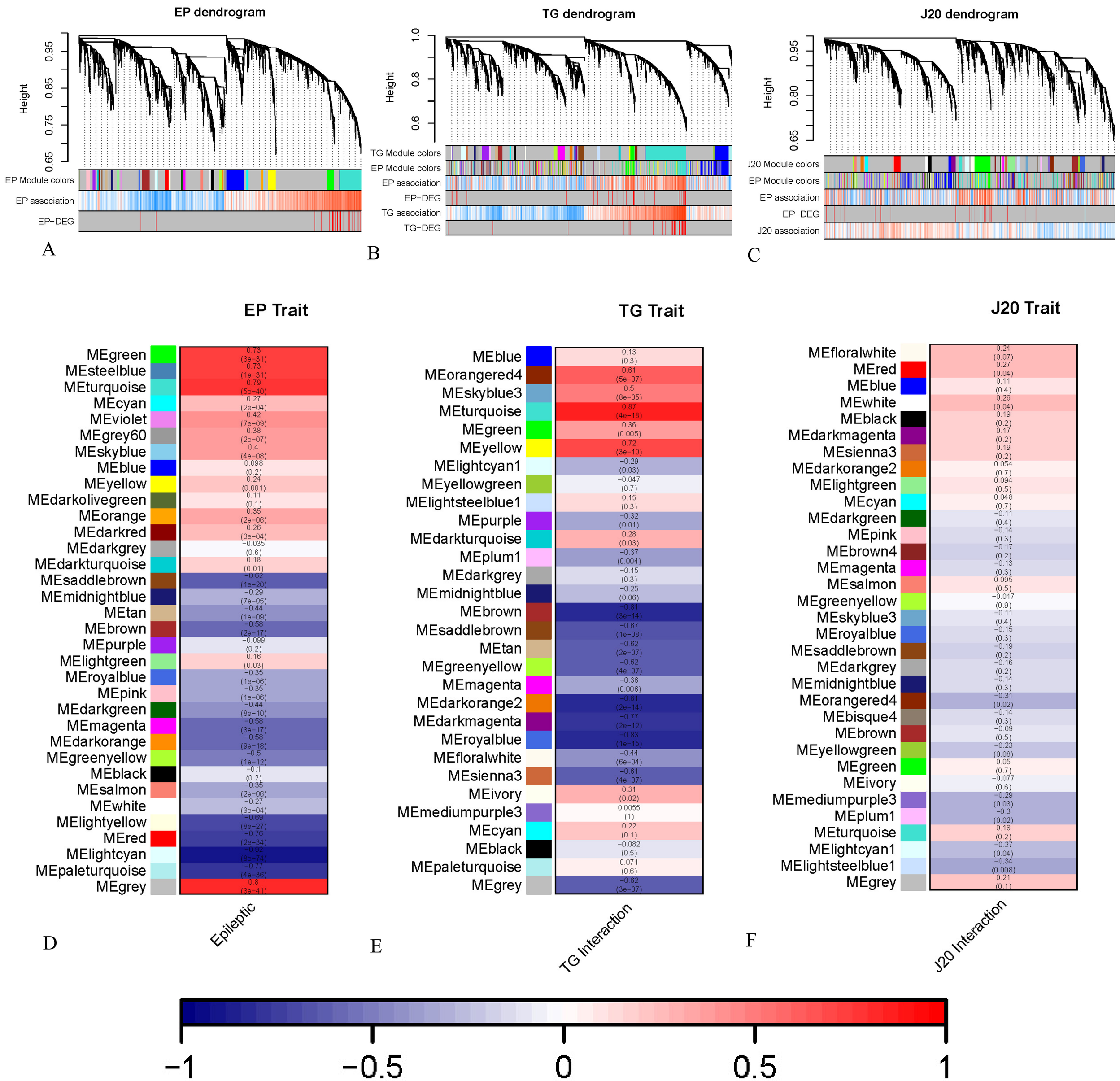
EP dendrogram
Height
0.65
0.75
0.85
0.95
EP Module colors
EP association
EP-DEG
A
TG dendrogram
Height
0.6
0.8
1.0
TG Module colors
EP Module colors
EP association
EP-DEG
TG association
TG-DEG
B
J20 dendrogram
Height
0.65
0.80
0.95
J20 Module colors
EP Module colors
EP association
EP-DEG
J20 association
C
EP Trait
MEgreen 0.73 (3e-31)
MEsteelblue 0.73 (1e-31)
MEturquoise 0.79 (5e-40)
MEcyan 0.27 (2e-04)
MEviolet 0.42 (7e-09)
MEgrey60 0.38 (2e-07)
MEskyblue 0.4 (4e-08)
MEblue 0.098 (0.2)
MEyellow 0.24 (0.001)
MEdarkolivegreen 0.11 (0.1)
MEorange 0.35 (2e-06)
MEdarkred 0.26 (3e-04)
MEdarkgrey -0.035 (0.6)
MEdarkturquoise 0.18 (0.01)
MEsaddlebrown -0.62 (1e-20)
MEmidnightblue -0.29 (7e-05)
MEtan -0.44 (1e-09)
MEbrown -0.58 (2e-17)
MEpurple -0.099 (0.2)
MElightgreen 0.16 (0.03)
MEroyalblue -0.35 (1e-06)
MEpink -0.35 (1e-06)
MEdarkgreen -0.44 (8e-10)
MEmagenta -0.58 (3e-17)
MEdarkorange -0.58 (9e-18)
MEgreenyellow -0.5 (1e-12)
MEblack -0.1 (0.2)
MEsalmon -0.35 (2e-06)
MEwhite -0.27 (3e-04)
MElightyellow -0.69 (8e-27)
MEred -0.76 (2e-34)
MElightcyan -0.92 (8e-74)
MEpaleturquoise -0.77 (4e-36)
MEgrey 0.8 (3e-41)
Epileptic
D
TG Trait
MEblue 0.13 (0.3)
MEorangered4 0.61 (5e-07)
MEskyblue3 0.5 (8e-05)
MEturquoise 0.87 (4e-18)
MEgreen 0.36 (0.005)
MEyellow 0.72 (3e-10)
MElightcyan1 -0.29 (0.03)
MEyellowgreen -0.047 (0.7)
MElightsteelblue1 0.15 (0.3)
MEpurple -0.32 (0.01)
MEdarkturquoise 0.28 (0.03)
MEplum1 -0.37 (0.004)
MEdarkgrey -0.15 (0.3)
MEmidnightblue -0.25 (0.06)
MEbrown -0.81 (3e-14)
MEsaddlebrown -0.67 (1e-08)
MEtan -0.62 (2e-07)
MEgreenyellow -0.62 (4e-07)
MEmagenta -0.36 (0.006)
MEdarkorange2 -0.81 (2e-14)
MEdarkmagenta -0.77 (2e-12)
MEroyalblue -0.83 (1e-15)
MEfloralwhite -0.44 (6e-04)
MEsienna3 -0.61 (4e-07)
MEivory 0.31 (0.02)
MEmediumpurple3 0.0055 (1)
MEcyan 0.22 (0.1)
MEblack -0.082 (0.5)
MEpaleturquoise 0.071 (0.6)
MEgrey -0.62 (3e-07)
TG Interaction
E
J20 Trait
MEfloralwhite 0.24 (0.07)
MEred 0.27 (0.04)
MEblue 0.11 (0.4)
MEwhite 0.26 (0.04)
MEblack 0.19 (0.2)
MEdarkmagenta 0.17 (0.2)
MEsienna3 0.19 (0.2)
MEdarkorange2 0.054 (0.7)
MElightgreen 0.094 (0.5)
MEcyan 0.048 (0.7)
MEdarkgreen -0.11 (0.4)
MEpink -0.14 (0.3)
MEbrown4 -0.17 (0.2)
MEmagenta -0.13 (0.3)
MEsalmon 0.095 (0.5)
MEgreenyellow -0.017 (0.9)
MEskyblue3 -0.11 (0.4)
MEroyalblue -0.15 (0.3)
MEsaddlebrown -0.19 (0.2)
MEdarkgrey -0.16 (0.2)
MEmidnightblue -0.14 (0.3)
MEorangered4 -0.31 (0.02)
MEbisque4 -0.14 (0.3)
MEbrown -0.09 (0.5)
MEyellowgreen -0.23 (0.08)
MEgreen 0.05 (0.7)
MEivory -0.077 (0.6)
MEmediumpurple3 -0.29 (0.03)
MEplum1 -0.3 (0.02)
MEturquoise 0.18 (0.2)
MElightcyan1 -0.27 (0.04)
MElightsteelblue1 -0.34 (0.008)
MEgrey 0.21 (0.1)
J20 Interaction
F
-1
-0.5
0
0.5
1

Figure 2

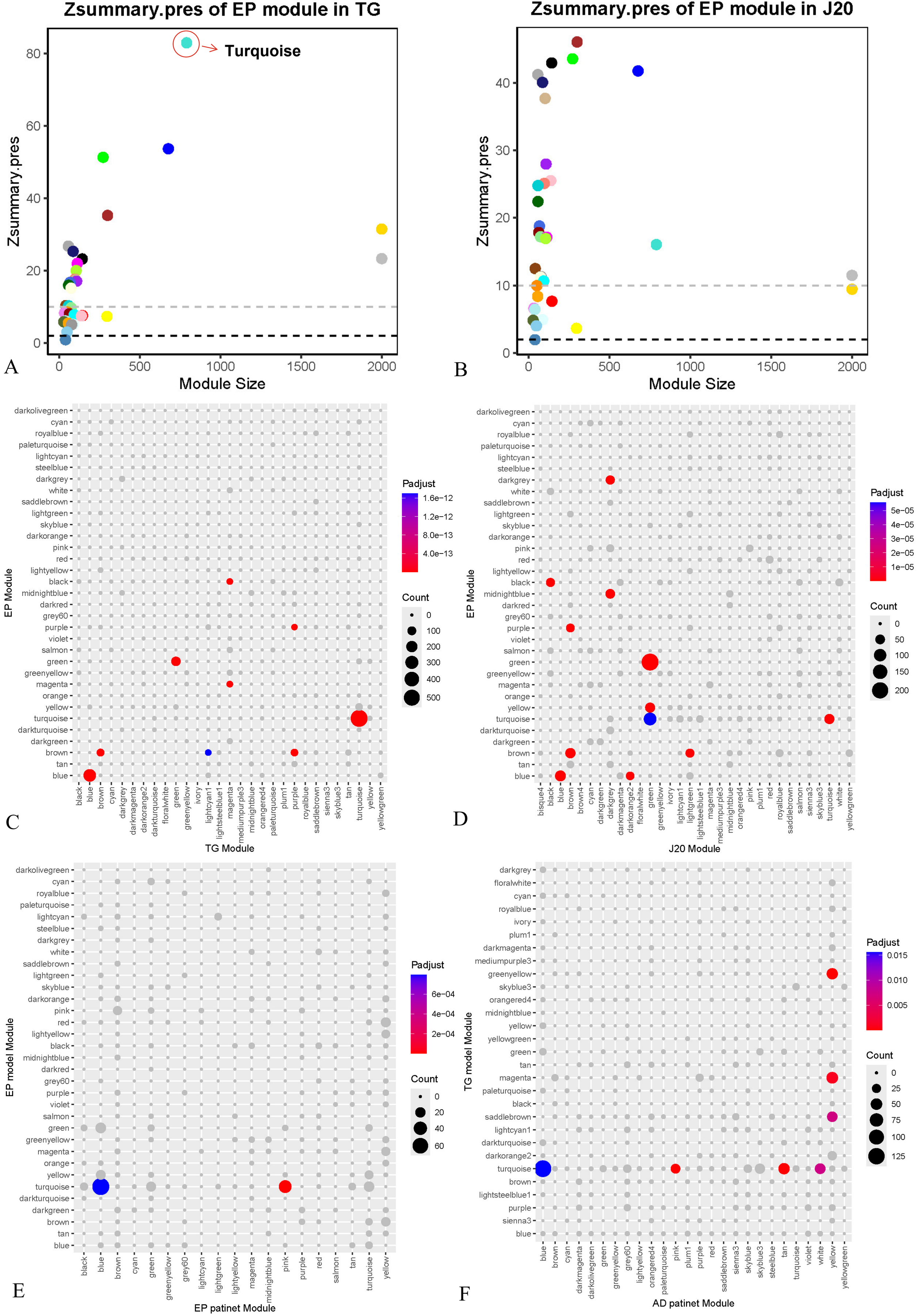
Zsummary.pres of EP module in TG
Turquoise
Zsummary.pres
Module Size
A
Zsummary.pres of EP module in J20
Zsummary.pres
Module Size
B
EP Module
TG Module
Padjust
Count
C
EP Module
J20 Module
Padjust
Count
D
EP model Module
EP patinet Module
Padjust
Count
E
TG model Module
AD patinet Module
Padjust
Count
F

Figure 3

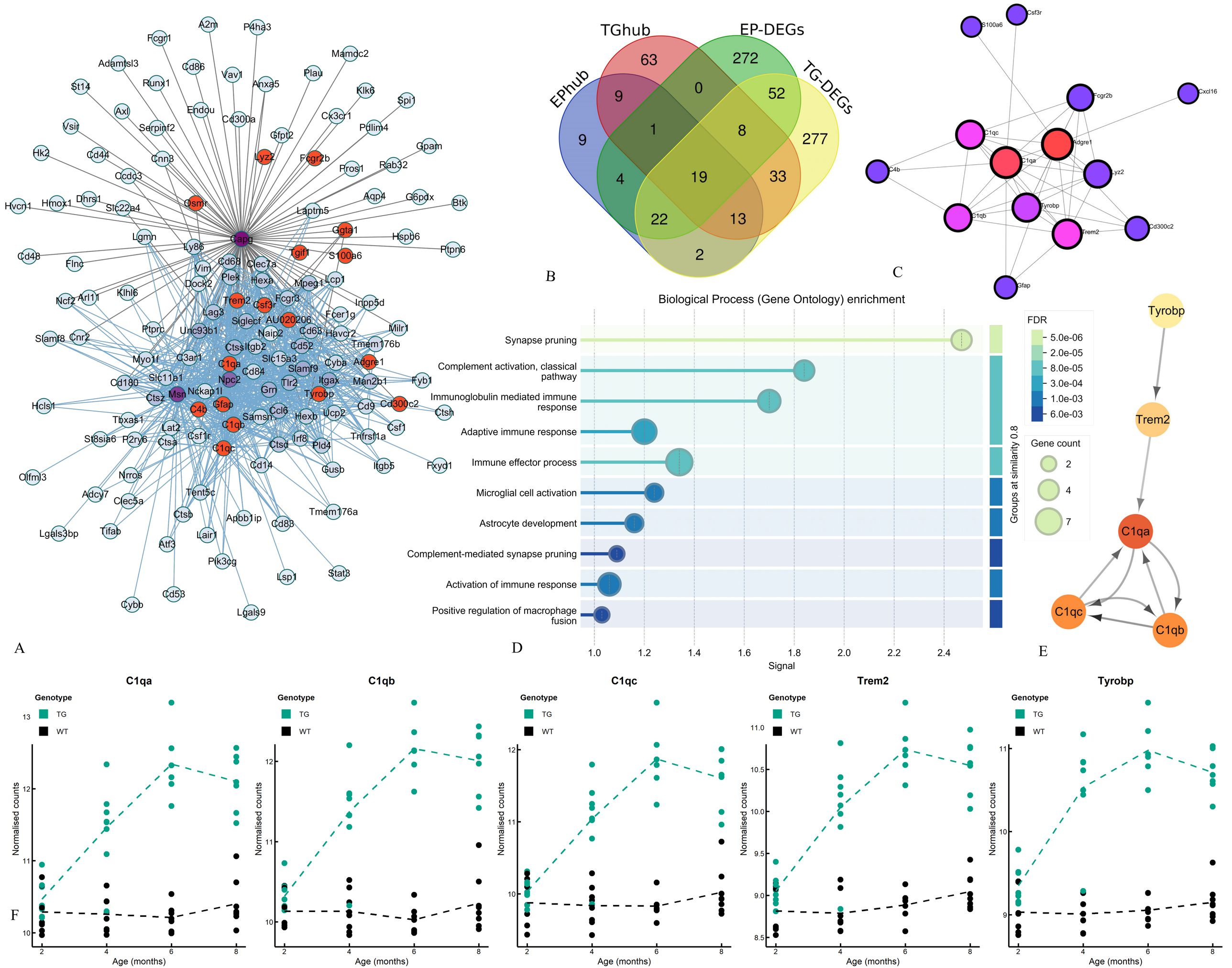

A
B
C
D
E
F
TGhub
EP-DEGs
EPhub
TG-DEGs
63
272
9
0
52
9
1
8
277
4
19
33
22
13
2
Biological Process (Gene Ontology) enrichment
Synapse pruning
Complement activation, classical pathway
Immunoglobulin mediated immune response
Adaptive immune response
Immune effector process
Microglial cell activation
Astrocyte development
Complement-mediated synapse pruning
Activation of immune response
Positive regulation of macrophage fusion
Groups at similarity 0.8
Signal
FDR
5.0e-06
2.0e-05
8.0e-05
3.0e-04
1.0e-03
6.0e-03
Gene count
2
4
7
Tyrobp
Trem2
C1qa
C1qc
C1qb
C1qa
C1qb
C1qc
Trem2
Tyrobp
Genotype
TG
WT
Normalised counts
Age (months)

Figure 4

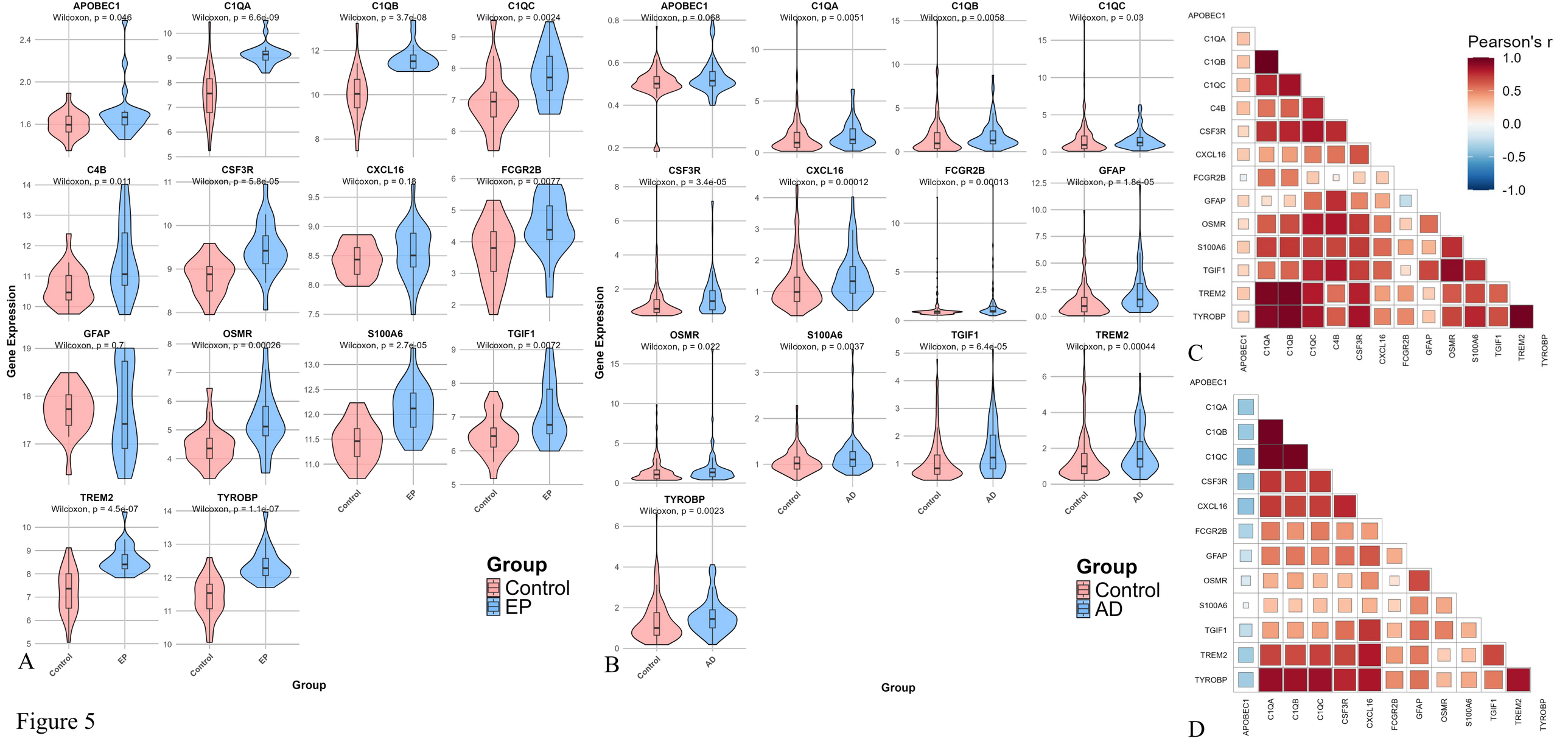
APOBEC1
Wilcoxon, p = 0.046
C1QA
Wilcoxon, p = 6.6e-09
C1QB
Wilcoxon, p = 3.7e-08
C1QC
Wilcoxon, p = 0.0024
C4B
Wilcoxon, p = 0.011
CSF3R
Wilcoxon, p = 5.8e-05
CXCL16
Wilcoxon, p = 0.18
FCGR2B
Wilcoxon, p = 0.0077
GFAP
Wilcoxon, p = 0.7
OSMR
Wilcoxon, p = 0.00026
S100A6
Wilcoxon, p = 2.7e-05
TGIF1
Wilcoxon, p = 0.0072
TREM2
Wilcoxon, p = 4.5e-07
TYROBP
Wilcoxon, p = 1.1e-07
Gene Expression
Control
EP
Group
Control
EP
A
APOBEC1
Wilcoxon, p = 0.068
C1QA
Wilcoxon, p = 0.0051
C1QB
Wilcoxon, p = 0.0058
C1QC
Wilcoxon, p = 0.03
CSF3R
Wilcoxon, p = 3.4e-05
CXCL16
Wilcoxon, p = 0.00012
FCGR2B
Wilcoxon, p = 0.00013
GFAP
Wilcoxon, p = 1.8e-05
OSMR
Wilcoxon, p = 0.022
S100A6
Wilcoxon, p = 0.0037
TGIF1
Wilcoxon, p = 6.4e-05
TREM2
Wilcoxon, p = 0.00044
TYROBP
Wilcoxon, p = 0.0023
Gene Expression
Control
AD
Group
Control
AD
B
Pearson's r
1.0
0.5
0.0
-0.5
-1.0
APOBEC1
C1QA
C1QB
C1QC
C4B
CSF3R
CXCL16
FCGR2B
GFAP
OSMR
S100A6
TGIF1
TREM2
TYROBP
C
D

Figure 5

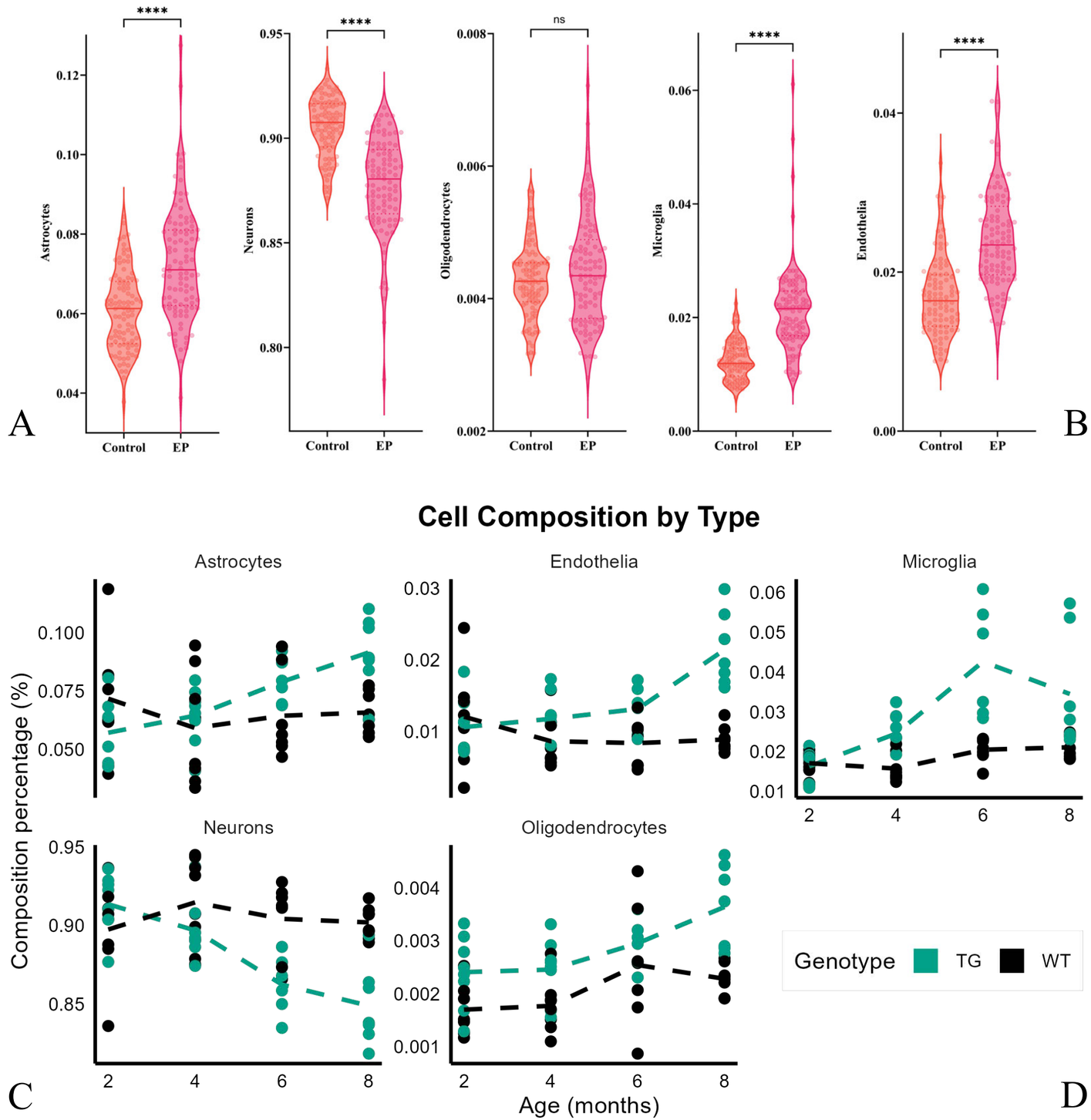
A
Astrocytes
Neurons
Oligodendrocytes
Microglia
Endothelia
Control
EP
****
ns
Cell Composition by Type
Composition percentage (%)
Age (months)
Genotype
TG
WT
C

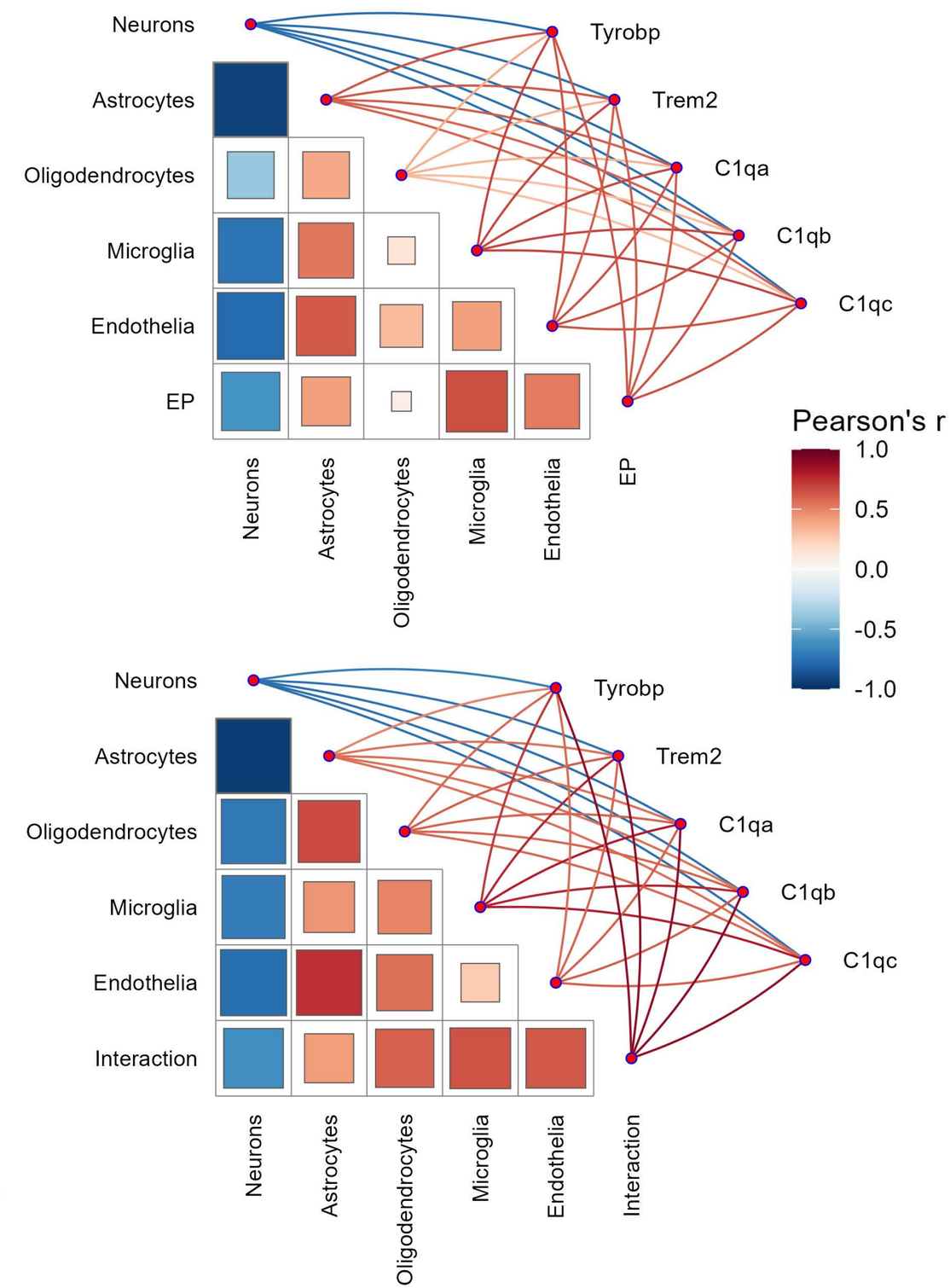
B
Neurons
Astrocytes
Oligodendrocytes
Microglia
Endothelia
EP
Tyrobp
Trem2
C1qa
C1qb
C1qc
Pearson's r
1.0
0.5
0.0
-0.5
-1.0
Interaction
D

Figure 6

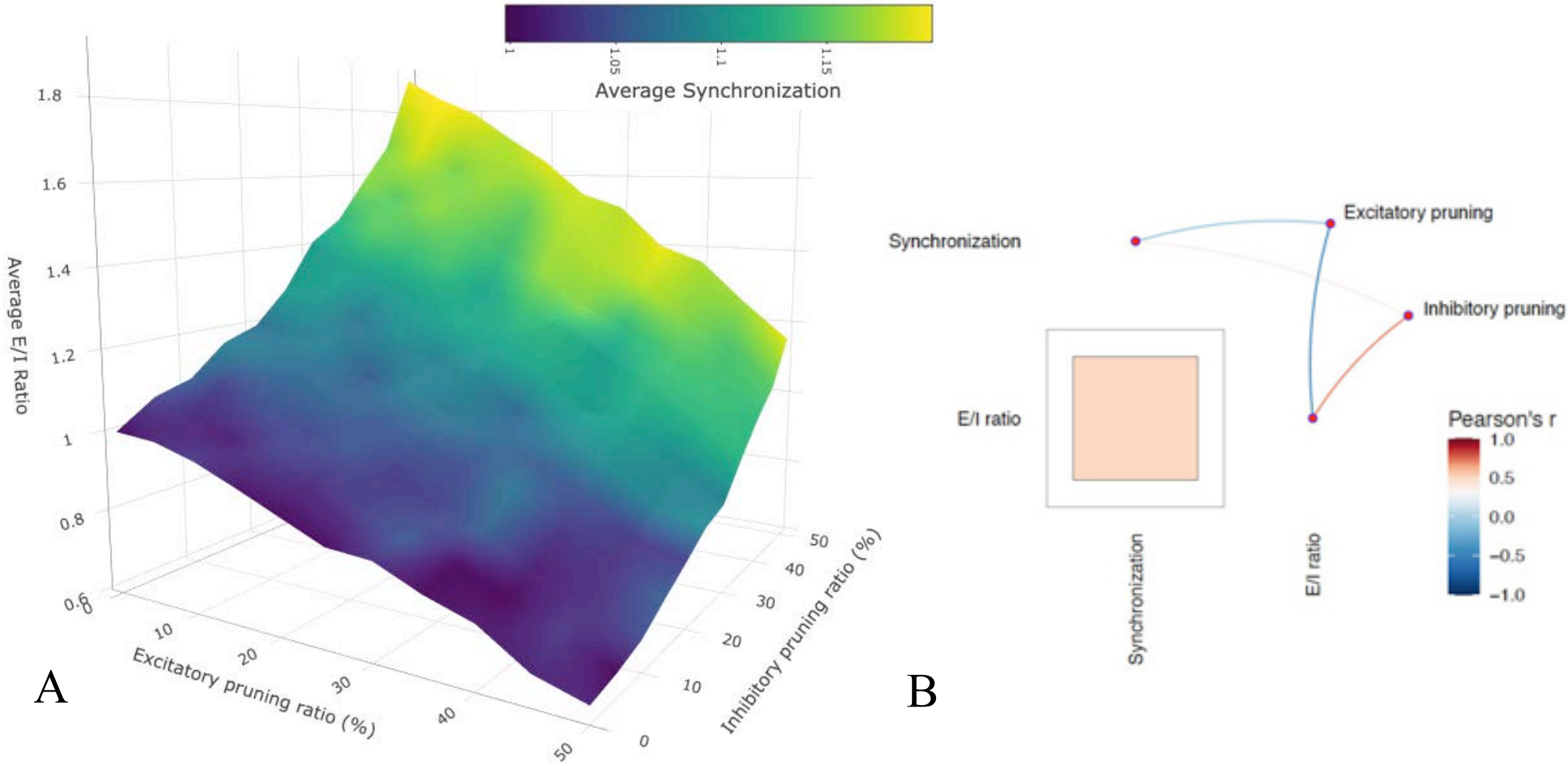
Average Synchronization
1
1.05
1.1
1.15
Average E/I Ratio
1.8
1.6
1.4
1.2
1
0.8
0.6
Excitatory pruning ratio (%)
0
10
20
30
40
50
Inhibitory pruning ratio (%)
0
10
20
30
40
50
A
Synchronization
Excitatory pruning
Inhibitory pruning
E/I ratio
Synchronization
E/I ratio
Pearson's r
1.0
0.5
0.0
−0.5
−1.0
B

Figure 7